BNL-216054-2020-JAAM

Probing Sources of Capacity Fade in LiNi0.6Mn0.2Co0.2O2 (NMC622): An Operando XRD Study of Li/NMC622 Batteries During Extended Cycling

C. D. Quilty, A. C. Marschilok

To be published in "JOURNAL OF PHYSICAL CHEMISTRY C"

April 2020

Interdisciplinary Science Department

Brookhaven National Laboratory

U.S. Department of Energy

USDOE Office of Science (SC), Basic Energy Sciences (BES) (SC-22)

Notice: This manuscript has been authored by employees of Brookhaven Science Associates, LLC under Contract No. DE-SC0012704 with the U.S. Department of Energy. The publisher by accepting the manuscript for publication acknowledges that the United States Government retains a non-exclusive, paid-up, irrevocable, world-wide license to publish or reproduce the published form of this manuscript, or allow others to do so, for United States Government purposes.

DISCLAIMER

This report was prepared as an account of work sponsored by an agency of the United States Government. Neither the United States Government nor any agency thereof, nor any of their employees, nor any of their contractors, subcontractors, or their employees, makes any warranty, express or implied, or assumes any legal liability or responsibility for the accuracy, completeness, or any third party's use or the results of such use of any information, apparatus, product, or process disclosed, or represents that its use would not infringe privately owned rights. Reference herein to any specific commercial product, process, or service by trade name, trademark, manufacturer, or otherwise, does not necessarily constitute or imply its endorsement, recommendation, or favoring by the United States Government or any agency thereof or its contractors or subcontractors. The views and opinions of authors expressed herein do not necessarily state or reflect those of the United States Government or any agency thereof.

Probing Sources of Capacity Fade in $LiNi_{0.6}Mn_{0.2}Co_{0.2}O_2$ (NMC622): An *Operando* XRD Study of Li/NMC622 Batteries During Extended Cycling

Calvin D. Quilty[1], David C. Bock[2], Shan Yan[2], Kenneth J. Takeuchi[1,3], Esther S. Takeuchi[1,2,3], Amy C. Marschilok[1,2,3]*

[1]Department of Chemistry, Stony Brook University, Stony Brook, New York 11794, United States
[2]Energy and Photon Sciences Directorate, Brookhaven National Laboratory, Upton, New York 11973, United States
[3]Department of Materials Science and Chemical Engineering, Stony Brook University, Stony Brook, New York 11794, United States

Abstract

$LiNi_{0.6}Mn_{0.2}Co_{0.2}O_2$ (NMC622) is one of the most promising Li-ion battery cathodes as it delivers high capacity at high potentials. However high potentials also lead to decreases in capacity retention where the disintegration of the secondary particles has been implicated as a major driving force of this capacity fade. This has been attributed to anisotropic lattice changes and increased microstrain during cycling. To probe how these factors affect capacity fade, Li/NMC622 batteries were cycled from 3-4.3 or 4.7 V and probed with *operando* X-ray diffraction over the 1st, 2nd, and 101st cycles. Further characterization with scanning electron microscopy, and inductively coupled plasma-optical emission spectroscopy was also performed. The use of *operando* XRD over many cycles allowed for the collection of detailed structural information in real time over a time frame in which fading can be observed. During the first two cycles, the cells

charged to 4.7 V exhibit increased anisotropic lattice changes as compared to the cells charged to 4.3 V. Upon the 101st cycle, when significant fade has been observed, the cells charged to 4.3 and 4.7 V show identical lattice changes to one another, while the 4.7 V charge limit induces more microstrain. This shows that elevated microstrain at high charge limits is a major driver for particle disintegration in NMC622 cathodes. This study provides important insights into the mechanisms of particle disintegration and capacity fade in NMC/Li-ion batteries, which will enable the design of NMC electrodes that deliver both higher capacities and exhibit better capacity retention.

Introduction

Lithium nickel manganese cobalt oxide (NMC, $LiNi_xMn_yCo_zO_2$ where $x+y+z=1$) is a promising lithium-ion battery cathode material due to its high reversibility, good practical capacity, and high energy.[1-6] Much of the initial research on NMC materials studied the NMC111 ($LiNi_{1/3}Mn_{1/3}Co_{1/3}O_2$) chemistry, also referred to as NMC333 where the 3 digits generally represent the ratio of the three transition metals. In this system, Ni is divalent, cobalt is trivalent, and manganese is tetravalent. In recent years, Ni rich NMC materials, where $x>y$, z and both di- and trivalent nickel are present, have generated significant interest because of higher capacity and energy density as well as reduced concentration of cobalt, which is relatively scarce.[7-12]

NMC is a layered, ordered rocksalt (**Figure S1a**) that is isostructural to α-$NaFeO_2$.[7, 13] NMC can be understood as a solid solution of $LiCoO_2$, $LiMnO_2$, and $LiNiO_2$ or of $LiCoO_2$ and $LiNi_{1/2}Mn_{1/2}O_2$.[2, 7, 14] NMC crystallizes in a hexagonal $R\bar{3}m$ space group (a = 2.860 Å, c = 14.227 Å, V = 100.76 Å^3).[7] It is characterized by alternating AB layers

along the *c* axis, where layer A consists of LiO_6 octahedra with lithium residing in Wyckoff site 3a and O in site 6c, and layer B is made up of MO_6 (*M* = Ni, Co, and Mn) where the *M* and O reside in the 3b and 6c sites respectively; the LiO_6 and MO_6 octahedra are connected by edge sharing linkages through their shared oxide ions (**Figure S1a**).[7] This NMC structure is designated as O3 in Delmas' notation as the lithium coordination is octahedral and the unit cell is defined by three MO_6 layers.[15] These relatively open lithium layers allow for high Li-ion conductivity which contributes to the rate capability of NMC as a Li-ion battery cathode.[16-17]

Although increasing the nickel content of NMC formulations offers an appealing increase in capacity and energy density as well as a cost reduction, it can worsen the problem of lithium-nickel site disorder.[8] Octahedral Ni^{2+} has a similar ionic radius to octahedral Li^{+}, 0.69 Å *vs*. 0.76 Å, while Mn^{4+}, Ni^{3+}, and Co^{3+} have significantly smaller radii of 0.53 Å, 0.60, and 0.61 Å respectively.[18] Due to their similar radii, Li^{+} and Ni^{2+} can exchange crystallographic sites. In a disordered structure, a certain percentage of Li^{+} moves to the 3b site while an equal amount of Ni^{2+} moves to the 3a site (**Figure S2**); for example, an NMC111 material with 5% disorder would have $Li_{0.95}Ni_{0.05}$ at site 3a and $Li_{0.05}Ni_{0.283}Co_{0.333}Mn_{0.333}$ at site 3b. This disorder becomes more significant with higher nickel content, increasing from ~3% for NMC111 to ~6% for NMC442 to ~7% for NMC811.[4, 8, 19-20] This disorder can have negative consequences on electrochemistry as nickel ions in the LiO_6 layer can block the diffusion pathways for lithium ions. The presence of nickel in the 3a site in the LiO_6 layer therefore can slow lithium diffusion and decrease the rate capability of the battery.[8]

Delithiation of NMC, both chemically and electrochemically, can result in several structural changes to the parent material; typically, these structural changes become most significant at high charge voltage when delithiation is pronounced.[5, 7, 21-22] These phases are designated H1, H2, and H3, where the H stands for hexagonal and the number indicates a series with increasing structural distortion (**Figure S1**).[23] These three phases have varying unit cells, but crystallize in the same space group ($R\bar{3}m$). H1 NMC is undistorted and is the structure of undischarged $LiNi_{0.6}Mn_{0.2}Co_{0.2}O_2$ (NMC622). Upon delithiation to $Li_{\sim 0.6}$, it is converted to H2 NMC622 which is isostructural but has a contracted *a* axis and expanded *c* axis. Further delithiation to $Li_{\sim 0.3}$ leads to H3 NMC622 which has a shorter *c* dimension. H3 NMC has a significantly lower unit cell volume than the other two phases leading to substantial capacity fade during cycling when this phase is accessed possibly due to the repeated anisotropic lattice changes that volume change entails.[5] The implication of these phase changes is that while higher voltage limits (*e.g.* ~4.7 V) may deliver more capacity initially upon charge than lower voltage limits (*e.g.* ~4.3 V) this capacity increase will be lost over cycling due to the increased fade from more significant structural changes.[5, 7]

Operando X-ray diffraction (XRD) is one of the most powerful techniques for obtaining structural information about crystalline battery materials as the cell operates. To this end, various NMC materials have been studied in lithium batteries using *operando* XRD.[3-5, 24] Tian *et al.* found that when NMC622/Li is cycled once from 2.5-4.7 V H1 NMC is reversibly converted to H2 NMC[5], although it should be noted that there was a significant *c* axis contraction near the end of charge in the H2 phase, *c* = ~14.46→~13.94 Å, indicating that some H3 NMC is produced at high states of charge.

This study determined the phases present based on unit cells obtained from the peak positions; detailed refinement information was not provided. In two studies by Kondrakov *et al.,* NMC111 and NMC811 ($LiNi_{0.8}Mn_{0.1}Co_{0.1}O_2$) *vs.* Li were cycled either once or twice and all of the data was fit with Rietveld refinement.[3-4] The studies found that when cycled from 3-4.3 V, NMC111 experiences a reversible *a* axis contraction and *c* axis expansion, while NMC811 additionally experiences a *c* axis contraction at high charge.[4] Multiple phases were not considered in this study, but these changes are consistent with reversible H1⇌H2 and H1⇌H2⇌H3 transitions respectively. Furthermore, NMC111 was found to have a gradual reversible increase in microstrain during charge while NMC811 was found to have more severe periodic buildups of strain during charging.[4] The authors suggest that this increase in microstrain and more severe lattice change results in the observed capacity fade due to particle pulverization.

NMC materials often aggregate in micron-scale spherical secondary particles; the breakdown of these particles due to repetitive anisotropic lattice changes and increases in microstrain upon charge[4, 25] has been suggested to be a major causal factor toward capacity fade.[4, 26-28] In the case of NMC, prior XRD studies have focused on either *ex situ* characterization after extended cycling or *operando* characterization for early cycling to show how lattice changes and strain induce particle cracking and as a result capacity fade.[4, 27-28] The usage of *operando* XRD over extended cycling allows for the observation of fading and failure mechanisms in real time and over realistic use conditions; however, there are few studies using *operando* XRD to study NMC materials over extended cycling and they generally use a moderate upper voltage limit (4.2-4.3 V).[29-31] Min *et al.* collected *operando* XRD of $LiNi_{0.91}Mn_{0.03}Co_{0.06}O_2$ cycled once, 50, and

100 times at a range of 3-4.3 V; in that study only unit cell information (*a*,*c*, and *V*) was extracted from the data.[30] Schweidler *et al.* performed more detailed structural refinements on $LiNi_{0.85}Mn_{0.05}Co_{0.1}O_2$ cycled 750x in a voltage range of 2.8-4.2 V, although no treatment of microstrain was presented.[29] Neudeck *et al.* performed *operando* XRD on a Li/NMC622 cell where the cathode had been previously cycled in a NMC622/graphite cell 1400 times; this *operando* experiment was limited to the discharge to 2.8 V from an open circuit potential of ~4.25 V and only unit cell information was considered.[31]

This paper outlines a study of the Ni rich NMC622 as a cathode in a lithium metal anode battery cycled extensively (~100 times) with structural evolution monitored by *operando* XRD. The cells are cycled to either a moderate (4.3 V *vs.* Li^+/Li) or a high (4.7 V *vs.* Li^+/Li) upper potential limit to determine how the NMC structure is affected by potentials known to induce high structural distortion in particular after significant cycling. All data were fit using the Rietveld method to ensure quantitative results were obtained. This study presents key quantitative structural information such as unit cells, phase fractions, and microstrain of the H1-H3 phases of NMC obtained in real time as a function of both charge potential limit and cycle number. Complementary electron microscopy was collected to evaluate morphological changes in the material under the two conditions. To our knowledge, this report is the first to study extended cycling of NMC622 at high voltages (*i.e.* > 4.3 V) using *operando* XRD and the first to quantify the associated changes in microstrain over extended cycling.

Experimental Section

Materials Characterization. Scanning electron microscopy (SEM) images were collected on a JEOL JSM-6010PLUS/LA microscope with an accelerating voltage of 5-15 kV. Inductively coupled plasma-optical emission spectroscopy (ICP-OES) was performed on a Thermo Scientific iCAP 6000 series instrument to confirm the stoichiometry of the NMC622 material. *Ex situ* X-ray powder diffraction (XRD) measurements were collected on a Rigaku Miniflex X-ray diffractometer with a 600 W Cu Kα X-ray source equipped with a Kβ filter and D/tex Ultra 1D detector.

Electrochemical Cell Fabrication. 2032 type coin cells were fabricated with NMC622 composite cathodes and lithium metal anodes in an argon filled glovebox. The NMC622 was purchased from Targray (99.6% pure) and used as received. The NMC composite cathode was formed by tape casting a slurry of 90% NMC622, 5% Super P carbon, and 5% polyvinylidene fluoride (PVDF) in N-methyl-2-pyrollidone onto a carbon coated aluminum foil (active mass = 11 mg/cm^2). The cells were constructed with cathode and anode separated by a polypropylene separator and 1 M $LiPF_6$ in 3:7 ethylene carbonate: dimethyl carbonate electrolyte. *Operando* XRD compatible pouch cells were fabricated in order to allow for sufficient X-rays to penetrate the cell housing for analysis. These cells used the same cell stack as the coin cells; however, the steel casing was replaced with a thin polypropylene pouch. The pouch cell fabrication was performed in a moisture controlled dry room (~100 ppm water vapor).

Electrochemical Testing. Cyclic voltammetry was performed using a Biologic VSP multichannel potentiostat from 3-4.3 and 4.7 V for three cycles at 0.1 mV/s. Galvanostatic cycling was performed on a MACCOR multichannel testing system and a Biologic VSP multichannel potentiostat at 30 °C. Coin cells were cycled 100 times over

either 3-4.3 V or 3-4.7 V *vs.* Li/Li^+ with a current density of 35 mA/g (C/5). Pouch cells were cycled from either 3-4.3 V or 3-4.7 V with a current density of 17.5 mA/g (C/10) with a one hour rest in between individual (dis)charges. *Operando* XRD data was collected on the pouch cells as described below. It should be noted that 175 mAh/g was used as the theoretical capacity, this capacity would result in delithiation upon charge to $Li_{0.34}Ni_{0.6}Mn_{0.2}Co_{0.2}O_2$

***Operando* X-ray Diffraction.** *Operando* XRD measurements were performed on pouch cells during electrochemical cycling using a Rigaku SmartLab X-ray diffractometer with a 1760 W Cu Kα X-ray source equipped with a Kβ filter and D/tex Ultra 1D detector. XRD measurements were collected from 16-70° 2θ with a step size of 0.05° and a scan speed of 2°/min. For the pouch cells fabricated with pre-cycled cathodes in order to collect *operando* XRD on the 101st cycle, the electrodes were recovered within an inert atmosphere glovebox, washed with pure dimethyl carbonate to remove any residual electrolyte salt, then transferred to the dry room for pouch cell fabrication. These electrodes experienced the same amount of exposure to the dry room environment as the pristine electrodes used to fabricate the pouch cells for cycle 1 *operando* measurements as the coin cells used for the first 100 cycles were fabricated in an inert atmosphere glove box.

Rietveld Refinements. Rietveld refinements of all patterns were performed with GSAS-II.[32] The region from ~20-30° 2θ was excluded from the fit as it contained intense polypropylene peaks and no signal associated with NMC622. The lithium foil anode was fit as a second phase ($Im\bar{3}m$, a = ~3.50 Å). Microstrain, observed through peak broadening, was fit with an isotropic microstrain parameter indicating uniform strain as

the use of multiple microstrain parameters did not yield stable fits.[33-34] Errors for unit cell parameters, phase fractions, and microstrain were determined from the GSAS-II fit results.

Results and Discussion

ICP-OES determined the stoichiometry of the NMC material to be $Li_{1.01}Ni_{0.61}Mn_{0.20}Co_{0.19}O_2$ confirming the NMC622 designation. SEM images of the NMC material are shown in **Figure 1A** and **B**. The NMC material is composed of large crystallites, on the order of 100s of nanometers, which aggregate into micron-scale secondary particles.

The structure of the pristine NMC622 material was characterized with XRD and the pattern was analyzed with Rietveld refinement to obtain detailed information about the structure. The fit and the structural information are shown in **Figure S3** and **Table 1** respectively. All of the peaks can be indexed to H1-NMC (space group = $R\bar{3}m$, *a* = 2.86 Å, *c* = 14.227 Å) with no detectable impurities. The unit cell and atomic positions are in good agreement with the literature.[7] The material is extremely crystalline and the structural strain is minimal. About 3% of the lithium and nickel have exchanged sites indicating that the disorder is low.[7]

Table 1. Structural information of NMC622 as obtained by Rietveld refinement.

Parameter	Value
a (Å)	2.86832(7)
c (Å)	14.21801(4)
Microstrain (%)	0.182(8)
Li/Ni site disorder (%)	3.1(5)
O(z)	0.2435(2)
% R_{wp}	2.17

In order to probe the structural evolution of the NMC622 material over the first, second, and 101st cycles, coin cells and *operando* XRD compatible pouch cells were fabricated with NMC622 as the cathode and lithium foil as the anode. *Operando* XRD data was collected on the pouch cells during the first two cycles. In parallel, coin cells were cycled one hundred times, the cathodes were recovered, and pouch cells were fabricated with those cathodes in order to collect *operando* XRD on the 101st cycle. Using this strategy, the structural evolutions of NMC622 were monitored *operando* for the formation cycle, an early cycle, and a cycle after extended cycling.

The coin cell cycling data is shown in **Figure 2**. The 4.7 V cell initially delivers higher charge and discharge capacities on the first cycle, 249 and 224 mAh/g, compared to 208 and 186 mAh/g for the 4.3 V cell. The decrease in capacity from the 1st charge to the 1st discharge is consistent with prior reports and has been attributed to electrolyte interface formation and kinetic limitations in the lithiation process.[35-36] On the other hand, the 4.7 V cell experiences significantly more capacity fade over 100 cycles, decreasing by 41% to 133 mAh/g by cycle 100; while, the 4.3 V cell only decreases 5.4% to 176 mAh/g. For both cells the Coulombic efficiency remains high; although it does decrease somewhat more for the 4.7 V cell, 94% compared to 98% at cycle 100. To ensure consistency, three additional coin cells were run at each potential limit; as shown in **Table S1**, the electrochemistry of the coin cells was reproducible, although there was more variability at the higher charge limit. Cyclic voltammetry (CV) data was collected on coin cells from 3-4.3 and 4.7 V (**Figure S4**). From 3-4.3 V, an oxidative peak is observed at 3.85 V and a reductive peak is observed at 3.65 V; these peaks are unchanged over cycling implying that a reversible phase transition is occurring. When

the window is expanded to 3-4.7 V a second pair of peaks is observed at 4.35 and 4.17 V respectively suggesting that a second phase change occurs at high potential.

The galvanostatic cycling for the pouch cells is shown in **Figure S5**. Similar to the coin cell data, the 1st cycle of the 4.7 V pouch cell delivers higher charge and discharge capacities than the 4.3 V cell, 223 and 169 mAh/g compared to 156 and 120 mAh/g, respectively. The lower delivered capacities compared to the coin cells is attributed to the somewhat lower stack pressure in the pouch cells. For the 101st cycle, the increased fade in the 4.7 V cell leads to the 4.3 V cell having a higher delivered charge capacity, 138 *vs*. 123 mAh/g. Overall, similar trends can be observed in the *operando* XRD pouch cells as were seen in the coin cells (**Figure S6**); therefore, the structural evolutions of NMC622 in a lithium battery could be studied using this method.

The XRD pattern of the pristine cell is shown in **Figure S7**; all of the expected NMC622 peaks in the 2θ window scanned can be observed as well as peaks from the cell components. The *operando* XRD patterns for cycles 1 and 2 for the 3-4.3 V and the 3-4.7 V cell are in **Figure 3**, and the *operando* XRD patterns for cycle 101 are shown in **Figure 4**. Significant, reversible changes can be observed upon (dis)charge from 3-4.3 V (**Figure 3** and **4 (top)**). The (003) peak shifts to lower angle upon charge while the (104) peak shifts to higher angle; these changes are reversed upon discharge and are still observed on cycle 101 although the shifting has lessened. These peak shifts suggest that there is a reversible contraction in the *a* parameter and an expansion in the *c* parameter during charge. This change is maintained, albeit to a slightly lesser extent, upon cycling. Notably, at intermediate levels of charge peak splitting is observed

indicating that phases of varying degrees of lithiation are present in both the discharge and the charge.

As would be expected, the 3-4.7 V cell looks quite similar to the 3-4.3 V cell over the portion of the voltage window in which they overlap for the first two cycles (**Figure 3** and **4(bottom)**). However, at potentials approaching 4.7 V during charge, there is a significant peak shift in the (003) and (104) peaks to higher angle. This change reverses upon discharge and indicates that at very high levels of charge there is a substantial contraction along the *c* axis of the material. Similarly, two phase regions can be observed here as well. Upon extended cycling, this high potential *c* axis contraction is no longer observed and the changes are quite similar to the 3-4.3 V cell.

In order to gain more quantitative information, Rietveld refinements were performed on all XRD patterns and the pertinent parameters are shown in **Figures 5 and 6.** The visual fits (select fits are shown in **Figures S8-23**) and goodness of fit parameters, $\%R_{wp,mean(SD)}$=4.1(4) (**Figure S24**), suggest that effective fitting has been accomplished across all patterns meaning, that reliable quantitative information can be extracted.

At the beginning of cycle 1, the 3-4.3 V cathode is composed of H1 NMC622 ($R\bar{3}m$, *a* = 2.86 Å, *c* = 14.227 Å). At ~3.8 V (~10 mAh/g) on the onset of the major voltage plateau (**Figure S5**), a second phase appears, H2 NMC ($R\bar{3}m$, *a* = 2.81 Å, *c* = 14.375 Å). The appearance of this phase is consistent with the *a* contraction and *c* expansion observed during charge. These phases coexist throughout the 1st charge, ultimately reaching an H1/H2 mixture of 27(6)/73(6)% (**Figure 5D**). The H2 weight fraction decreases upon discharge and disappears at ~3.6 V (~100 mAh/g) at the end of the

discharge voltage plateau. This H1⇌H1&H2⇌H1 transition occurs very similarly during cycles 2 and 101 (**Figures 5D** and **6D**). This shows that the structural evolution that occurs over the 3-4.3 V window is consistent over extended cycling.

On cycle 1 the 3-4.7 V cell initially undergoes a similar transition, then at ~4.3 V (~160 mAh/g) the H1&H2 mixture converts fully to the H2 phase (**Figure 5I**). At ~4.4 V (~180 mAh/g) a new phase appears, H3 NMC ($R\bar{3}m$, *a* = 2.82 Å, *c* = 13.67 Å); the appearance of this phase is the cause of the *c* axis contraction that is observed at high potential. The resulting mixture of H2&H3 is converted to pure H3 at ~4.6 V (~210 mAh/g) near the end of charge. These phase changes are sequentially reversed upon discharge until at ~3.6 V (~140 mAh/g) only H1 NMC remains, similar to what was observed in a prior report.[5] The phase evolutions for cycle 2 were quite similar; however, significant differences were observed for cycle 101 (**Figure 6I**). Upon charge the H1 NMC is converted to H1&H2 at ~3.8 V (~20 mAh/g) similar to the onset in the other cells, but no further transitions are observed in the cycle. It should be noted that due to the high level of capacity fade observed for this cell, the discharge was quite short which explains the lack of pure H1 at the end of the discharge.

As expected for a highly crystalline, pristine material the microstrain of NMC622 is quite low, ~0.40% prior to cycle one. During cycling significant changes are observed in the microstrain of the material. For the 3-4.3 V cell, the microstrain of the discharged states is low even after extended cycling; from the pristine state to the 101st discharged state the strain only increases to 0.49(3)% (**Figure 5E** and **Figure 6E**). As the cell charges, microstrain increases as previously reported[4]; this is driven by an increase in strain in the H1 phase. The H2 phase has essentially constant strain of ~0.5%, while H1

becomes more strained at high states of charge reaching maxima of 1.3(3), 1.6(3), and 1.8(3)% at charge at cycles 1, 2, & 101 respectively. In summary, the 3-4.3 V cell has moderate increases in strain at high states of charge that then reversibly decrease during discharge throughout the first 101 cycles, although there is a gradual increase in strain at high states of charge as the cell cycles.

The 3-4.7 V cell experiences significantly higher levels of strain during cycling. At the discharged state, H1 increases in strain during cycling to 0.52(3), 0.77(5), and 0.9(1)% at the end of discharge for cycles 1, 2, and 101 respectively (**Figure 5J** and **6J**). In addition, during the first two cycles, the microstrain of both the H1 and H2 phases increase to ~1.7% before converting to H2 and H3 respectively. Upon extended cycling the increase in strain becomes even more significant, at high levels of charge the H1 phase's microstrain increases dramatically ultimately reaching 2.6(2)% at full charge. Overall, the 3-4.7 V cell reaches higher microstrain values than the 3-4.3 V cell especially after cycling 100 times.

While initially the 3-4.7 V window delivers higher capacity, capacity fade is much more significant. Structural distortion likely plays a role here as from 3-4.3 V NMC622 undergoes a volume change of less than 3% while from 3-4.7 V the change is 7%. This cyclical distortion can break up the NMC622 particles which causes the electrode to lose electrical contact decreasing delivered capacity.[4, 26-28] However the data shows that the extent of these distortions is lessened during cycling meaning that other factors are critical. Specifically, microstrain is a larger factor in the observed fade in this system as cycling to the 4.7 V limit leads to substantially higher strain overall, and crucially this strain in fact increases over extended cycling. This shows that while structural changes

are likely a factor in higher voltage limit capacity fade in the NMC622 system, microstrain increase is the primary structural driving force.

To provide verification of the particle disintegration, SEM images of cycled cathodes were collected (**Figure 1C-I** and **S25**). After cycling 100 times at either 3-4.3 or 3-4.7 V, small holes form on the surface of the secondary particles. In the case of the 3-4.3 V cathode, these holes are the only visible changes across the cathode surface (**Figure 1C-E**, and **Figure S25A-D**). Further damage is observed in the cathode cycled in the larger voltage window; significant cracks can be seen through ~30% of the cathode (**Figure 1G and H**) in particular in the middle-left area of **Figure 1G** and the right side of **Figure 1H**. In addition, damage to the cathode cycled at 3-4.7 V is nonuniform; some locations on the cathode show minimal damage besides the appearance of holes (**Figure S25E** and **F**) while in other parts the secondary particles have entirely disintegrated (**Figure 1I** and **Figure S25G** and **H**). In contrast, the cathode cycled at 3-4.3 V is uniform with holes throughout the secondary particles but no significant cracking or particle disintegration observed on the surface. Cross sectional SEM images were collected to provide additional information in the interior of the cathodes (**Figure S26**). When cycled from 3-4.3 V, there is some particle disintegration in the interior of the electrode (**Figure S26C** and **D**) as compared to the pristine (**Figure S26A** and **B**) but the electrode remains dense and compact throughout. In contrast, when cycled to 3-4.7 V the electrode displays significant hollowed-out spots (**Figure S26E** and **F**) and micron-scale cracking (**Figure S26G-I**). As such the cross sectional SEM confirms that significantly more damage is done to the electrode when cycled from 3-4.7 V. Therefore, the SEM images corroborate the XRD findings suggesting that

secondary particle disintegration occurs more extremely at higher potentials, and this breakdown will lead to capacity fade consistent with prior results.[4, 26-28] In addition, the damage observed is consistent with the variability noted in the capacity fade (**Table S1**); the cracks and disintegration will reduce capacity significantly and the nonuniformity in where they occur is likely to cause some variation in how quickly individual cells fade.

Conclusions

Li/NMC622 cells were found to deliver 20% higher capacity upon charging to 4.7 V *vs.* Li/Li^+ then when charging to 4.3 V. However, these higher potential cells faded more significantly by the 100th cycle, 41% loss of capacity from cycle two to 100 compared to only 5% for the lower charge potential cells. To probe the structural changes behind these differences in capacity fade, *operando* XRD data were collected on NMC622/Li pouch cells cycled from either 3-4.7 V or 3-4.3 V *vs.* Li/Li^+ for the 1st, 2nd, and 101st cycles. For all cycles the 3-4.3 V cell reversibly converts from H1 NMC upon discharge to a mixture of H1&H2 upon charge. The 3-4.7 V cell initially undergoes a series of reversible transitions from H1 to H3 upon discharge to charge, but by cycle two these transitions lessens and on cycle 101 the material does not convert further than a mixture of H1&H2.

The 3-4.7 V cell also exhibits higher levels of microstrain upon charge than the 3-4.3 V cell; this is most pronounced upon extended cycling. Anisotropic changes in the lattice parameters certainly play a role in the increased fade experienced by NMC622/Li cells that are cycled with the larger 3-4.7 V potential window. However, the gradual loss of the highly distorted H3 phase over cycling at higher potential implies that additional factors are present as the higher potential cell continues to fade even as the lattice

changes become more similar to the 3-4.3 V cell. The dramatic increases in microstrain observed for the 3-4.7 V cell especially after extended cycling is a major factor in the observed capacity fade of NMC622 at higher potential charging. This capacity fade may occur because of disintegration of secondary particles brought on by the periodic buildup of strain in the crystallites; this disintegration is corroborated by the SEM images.

The observations made in this study will be important in designing next-generation battery materials with desirable physical properties that can avoid significant capacity fade and premature failure. The design of these materials will be crucial for allowing new batteries to be introduced to enable the widespread adoption in vehicles and grid level storage for renewable energy that is needed to power a sustainable future. This study highlights the power of *operando* battery testing over extended cycling to gain important structural information that can determine how the battery operates or fails to operate and could be applied to study many other relevant battery systems.

Associated Content

Supporting Information: Rietveld refinements, X-ray diffraction patterns, goodness of fit parameters, SEM images, coin and pouch cell electrochemistry, and crystal structures.

Author Information

Corresponding author: amy.marschilok@stonybrook.edu (ACM)

ORCID

Calvin D. Quilty: 0000-0002-0294-6815

Shan Yan: 0000-0002-9715-9100

David C. Bock: 0000-0002-2387-7791

Esther S. Takeuchi: 0000-0001-8518-1047

Kenneth J. Takeuchi: 0000-0001-8129-444X

Amy C. Marschilok: 0000-0001-9174-0474

Notes

The authors declare no competing financial interest.

Acknowledgements: The authors acknowledge Mercedes-Benz Research and Development North America (MBRDNA) for supporting the studies relevant to NMC. Development of the pouch cell assembly and testing methodology was supported as part of the Center for Mesoscale Transport Properties, an Energy Frontier Research Center funded by the U.S. Department of Energy, Office of Science, Basic Energy Sciences, under award #DE-SC0012673. The pouch cell assembly line was supported under award 75039 from the New York State Energy Research and Development Authority (NYSERDA) and award 76890 from the New York State Department of Economic Development (DED), which were provided as matching funds to the Center of Mesoscale Transport Properties. NYSERDA has not reviewed the information contained herein, and the opinions expressed do not necessarily reflect those of NYSERDA, or the State of New York. Any opinions, findings, conclusions, or recommendations expressed are those of the author(s) and do not necessarily reflect the views of the DED. The high magnification electron microscopy measurements used resources of the Center for Functional Nanomaterials, which is a U.S. DOE Office of Science Facility, at Brookhaven National Laboratory under Contract No. DE-

SC0012704. E.S.T. acknowledges support as the William and Jane Knapp Chair in Energy and the Environment.

References

1. Ohzuku, T.; Makimura, Y., Layered Lithium Insertion Material of LiCo1/3Ni1/3Mn1/3O2 for Lithium-Ion Batteries. *Chem. Lett.* **2001**, *7*, 642-643.

2. Lu, Z.; MacNeil, D. D.; Dahn, J. R., Layered Li[NixCo1-2xMnx]O2 Cathode Materials for Lithium-Ion Batteries. *Electrochem. Solid-State Lett.* **2001**, *4*, A200-A203.

3. Kondrakov, A. O.; Gesswein, H.; Galdina, K.; de Biasi, L.; Meded, V.; Filatova, E. O.; Schumacher, G.; Wenzel, W.; Hartmann, P.; Brezesinski, T., *et al.* Charge-Transfer-Induced Lattice Collapse in Ni-Rich Ncm Cathode Materials During Delithiation. *J. Phys. Chem. C* **2017**, *121*, 24381-24388.

4. Kondrakov, A. O.; Schmidt, A.; Xu, J.; Gesswein, H.; Moenig, R.; Hartmann, P.; Sommer, H.; Brezesinski, T.; Janek, J., Anisotropic Lattice Strain and Mechanical Degradation of High- and Low-Nickel NCM Cathode Materials for Li-Ion Batteries. *J. Phys. Chem. C* **2017**, *121*, 3286-3294.

5. Tian, C.; Nordlund, D.; Xin, H. L.; Xu, Y.; Liu, Y.; Sokaras, D.; Lin, F.; Doeff, M. M., Depth-Dependent Redox Behavior of LiNi0.6Mn0.2Co0.2O2. *J. Electrochem. Soc.* **2018**, *165*, A696-A704.

6. Menetrier, M.; Bains, J.; Croguennec, L.; Flambard, A.; Bekaert, E.; Jordy, C.; Biensan, P.; Delmas, C., NMR Evidence of LiF Coating Rather Than Fluorine Substitution in Li(Ni0.425Mn0.425Co0.15)O2. *J. Solid State Chem.* **2008**, *181*, 3303-3307.

7. Yin, S. C.; Rho, Y. H.; Swainson, I.; Nazar, L. F., X-Ray/Neutron Diffraction and Electrochemical Studies of Lithium De/Re-Intercalation in Li1-XCo1/3Ni1/3Mn1/3O2 (X = 0 → 1). *Chem. Mater.* **2006**, *18*, 1901-1910.

8. Tian, C.; Lin, F.; Doeff, M. M., Electrochemical Characteristics of Layered Transition Metal Oxide Cathode Materials for Lithium Ion Batteries: Surface, Bulk Behavior, and Thermal Properties. *Acct. Chem. Res.* **2018**, *51*, 89-96.

9. Radin, M. D.; Hy, S.; Sina, M.; Fang, C.; Liu, H.; Vinckeviciute, J.; Zhang, M.; Whittingham, M. S.; Meng, Y. S.; Van der Ven, A., Narrowing The Gap Between Theoretical and Practical Capacities in Li-Ion Layered Oxide Cathode Materials. *Adv. Energy Mater.* **2017**, *7*, 1602888/1-1602888/33.

10. Thackeray, M. M.; Croy, J. R.; Lee, E.; Gutierrez, A.; He, M.; Park, J. S.; Yonemoto, B. T.; Long, B. R.; Blauwkamp, J. D.; Johnson, C. S., *et al.* The Quest for

Manganese-Rich Electrodes for Lithium Batteries: Strategic Design and Electrochemical Behavior. *Sustainable Energy Fuels* **2018**, *2*, 1375-1397.

11. Li, H.; Li, J.; Ma, X.; Dahn, J. R., Synthesis of Single Crystal LiNi0.6Mn0.2Co0.2O2 with Enhanced Electrochemical Performance for Lithium Ion Batteries. *J. Electrochem. Soc.* **2018**, *165*, A1038-A1045.

12. Markevich, E.; Salitra, G.; Hartmann, P.; Kulisch, J.; Aurbach, D.; Park, K.-J.; Yoon, C. S.; Sun, Y.-K., New Insights Related to Rechargeable Lithium Batteries: Li Metal Anodes, Ni Rich LiNixCoyMnzO2 Cathodes and Beyond Them. *J. Electrochem. Soc.* **2019**, *166*, A5265-A5274.

13. Mather, G. C.; Dussarrat, C.; Etourneau, J.; West, A. R., A Review of Cation-Ordered Rock Salt Superstructure Oxides. *J. Mater. Chem.* **2000**, *10*, 2219-2230.

14. Koyama, Y.; Makimura, Y.; Tanaka, I.; Adachi, H.; Ohzuku, T. Systematic Research on Insertion Materials Based on Superlattice Models in a Phase Triangle of LiCoO2-LiNiO2-LiMnO2. *J. Electrochem. Soc.* **2004**, *151*, A1499-A1506.

15. Delmas, C.; Fouassier, C.; Hagenmuller, P., Structural Classification and Properties of The Layered Oxides. *Physica B+C (Amsterdam)* **1980**, *99*, 81-5.

16. Cui, S.; Wei, Y.; Liu, T.; Deng, W.; Hu, Z.; Su, Y.; Li, H.; Li, M.; Guo, H.; Duan, Y., *et al.* Optimized Temperature Effect of Li-Ion Diffusion with Layer Distance in Li(NixMnyCoz)O2 Cathode Materials for High Performance Li-Ion Battery. *Adv. Energy Mater.* **2016**, *6*, 1501309/1-1501309/9.

17. Wei, Y.; Zheng, J.; Cui, S.; Song, X.; Su, Y.; Deng, W.; Wu, Z.; Wang, X.; Wang, W.; Rao, M., *et al.* Kinetics Tuning of Li-Ion Diffusion in Layered Li(NixMnyCoz)O2. *J. Am. Chem. Soc.* **2015**, *137*, 8364-8367.

18. Shannon, R. D. Revised Effective Ionic Radii and Systematic Studies of Interatomic Distances in Halides and Chalcogenides. *Acta Crystallogr., Sect. A* **1976**, *A32*, 751-67.

19. Li, Z.; Chernova, N. A.; Roppolo, M.; Upreti, S.; Petersburg, C.; Alamgir, F. M.; Whittingham, M. S., Comparative Study of The Capacity and Rate Capability of LiNiyMnyCo1-2yO2 (Y = 0.5, 0.45, 0.4, 0.33). *J. Electrochem. Soc.* **2011**, *158*, A516-A522.

20. Van der Ven, A.; Ceder, G., Ordering in Lix(Ni0.5Mn0.5)O2 and Its Relation to Charge Capacity and Electrochemical Behavior in Rechargeable Lithium Batteries. *Electrochem. Commun.* **2004**, *6*, 1045-1050.

21. Ohzuku, T.; Ueda, A.; Nagayama, M., Electrochemistry and Structural Chemistry of Lithium Nickel Oxide (LiNiO2)(R$\bar{3}$M) for 4 Volt Secondary Lithium Cells. *J. Electrochem. Soc.* **1993**, *140*, 1862-70.

22. Li, W.; Reimers, J. N.; Dahn, J. R. In Situ X-Ray Diffraction and Electrochemical Studies of Li1-XNiO2. *Solid State Ionics* **1993**, *67*, 123-30.

23. Yoon, W.-S.; Chung, K. Y.; McBreen, J.; Yang, X.-Q., A Comparative Study on Structural Changes of LiCo1/3Ni1/3Mn1/3O2 and LiNi0.8Co0.15Al0.05O2 During First Charge Using in Situ XRD. *Electrochem. Commun.* **2006**, *8*, 1257-1262.

24. Xu, G.-L.; Liu, Q.; Lau, K. S.; Liu, Y.; Liu, X.; Gao, H.; Zhou, X.; Zhuang, M.; Ren, Y.; Li, J., *et al.* Building Ultraconformal Protective Layers on Both Secondary and Primary Particles of Layered Lithium Transition Metal Oxide Cathodes. *Nature Energy* **2019**, *4*, 484-494.

25. Fell, C. R.; Qian, D.; Carroll, K. J.; Chi, M.; Jones, J. L.; Meng, Y. S., Correlation Between Oxygen Vacancy, Microstrain, and Cation Distribution in Lithium-Excess Layered Oxides During the First Electrochemical Cycle. *Chem. Mater.* **2013**, *25*, 1621-1629.

26. Liu, H.; Wolf, M.; Karki, K.; Yu, Y.-S.; Stach, E. A.; Cabana, J.; Chapman, K. W.; Chupas, P. J., Intergranular Cracking as a Major Cause of Long-Term Capacity Fading of Layered Cathodes. *Nano Lett.* **2017**, *17*, 3452-3457.

27. Ishidzu, K.; Oka, Y.; Nakamura, T., Lattice Volume Change During Charge/Discharge Reaction and Cycle Performance of Li[NixCoyMnz]O2. *Solid State Ionics* **2016**, *288*, 176-179.

28. Lee, E.-J.; Chen, Z.; Noh, H.-J.; Nam, S. C.; Kang, S.; Kim, D. H.; Amine, K.; Sun, Y.-K., Development of Microstrain in Aged Lithium Transition Metal Oxides. *Nano Lett.* **2014**, *14*, 4873-4880.

29. Schweidler, S.; de Biasi, L.; Garcia, G.; Mazilkin, A.; Hartmann, P.; Brezesinski, T.; Janek, J., Investigation into Mechanical Degradation and Fatigue of High-Ni NCM Cathode Material: A Long-Term Cycling Study of Full Cells. *ACS Appl. Energy Mater.* **2019**, *2*, 7375-7384.

30. Min, K.; Jung, C.; Ko, D.-S.; Kim, K.; Jang, J.; Cho, E.; Park, K., High-Performance and Industrially Feasible Ni-Rich Layered Cathode Materials by Integrating Coherent Interphase. *ACS Appl. Mater. Interfaces* **2018**, *10*, 20599-20610.

31. Neudeck, S.; Mazilkin, A.; Reitz, C.; Hartmann, P.; Janek, J.; Brezesinski, T., Effect of Low-Temperature Al2O3 ALD Coating on Ni-Rich Layered Oxide Composite Cathode on the Long-Term Cycling Performance of Lithium-Ion Batteries. *Sci. Rep.* **2019**, *9*, 5328.

32. Toby, B. H.; Von Dreele, R. B., GSAS-II: The Genesis of a Modern Open-Source All Purpose Crystallography Software Package. *J. Appl. Crystallogr.* **2013**, *46*, 544-549.

33. Shafi, P. M.; Bose, A. C., Impact of Crystalline Defects and Size on X-Ray Line Broadening: A Phenomenological Approach for Tetragonal SnO2 Nanocrystals. *AIP Adv.* **2015**, *5*, 057137/1-057137/10.

34. Stephens, P. W. Phenomenological Model of Anisotropic Peak Broadening in Powder Diffraction. *J. Appl. Crystallogr.* **1999**, *32*, 281-289.

35. Xu, J.; Deshpande, R. D.; Pan, J.; Cheng, Y.-T.; Battaglia, V. S., Electrode Side Reactions, Capacity Loss and Mechanical Degradation in Lithium-Ion Batteries. *J. Electrochem. Soc.* **2015**, *162*, A2026-A2035.

36. Kasnatscheew, J.; Evertz, M.; Streipert, B.; Wagner, R.; Kloepsch, R.; Vortmann, B.; Hahn, H.; Nowak, S.; Amereller, M.; Gentschev, A.-C., *et al.* The Truth About the 1st Cycle Coulombic Efficiency of LiNi1/3Co1/3Mn1/3O2 (NCM) Cathodes. *Phys. Chem. Chem. Phys.* **2016**, *18*, 3956-3965.

Figures:

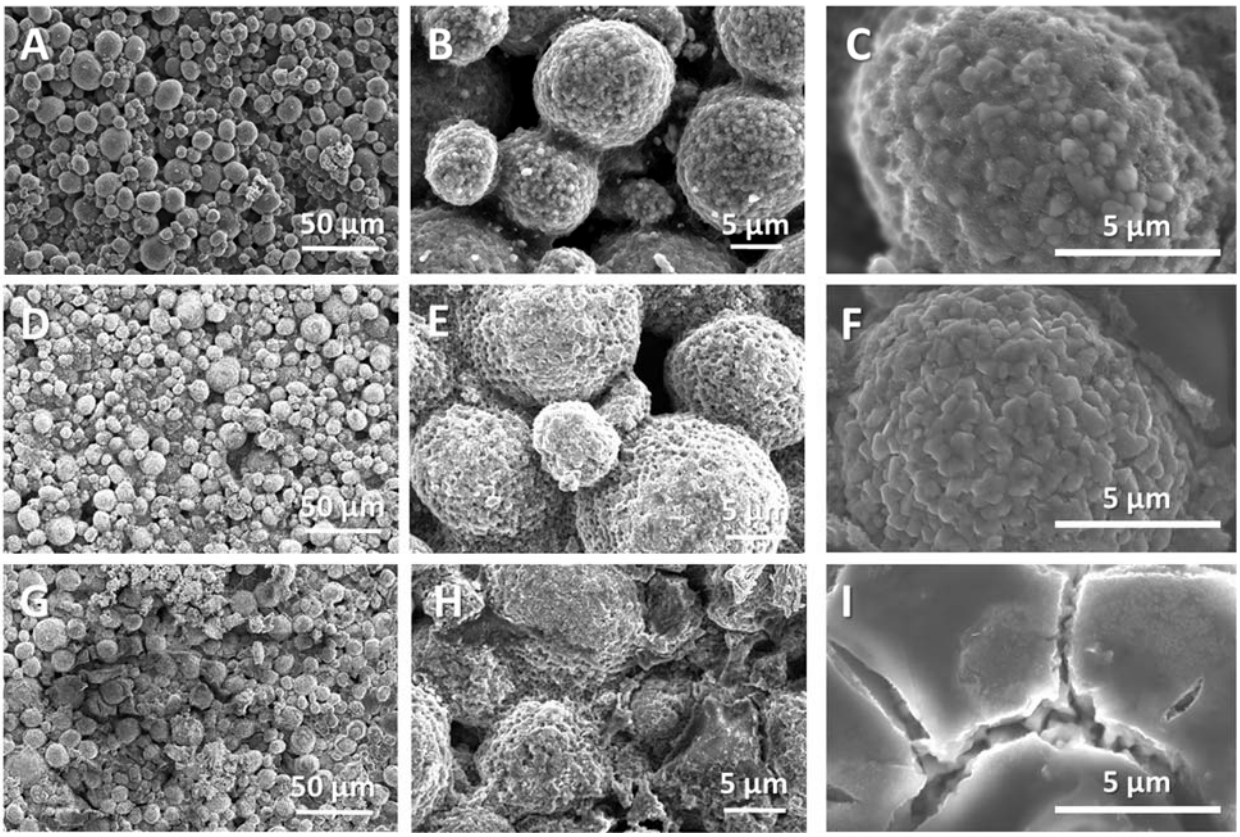

Figure 1. SEM images of a pristine NMC622 electrode at *(A)* 500X and *(B)* 4000X magnification. Images of an electrode cycled 100 times at 3-4.3 V at *(D)* 500X, *(E)* 4000X, and *(C) 10000X* magnification. Images of an electrode cycled 100 times at 3-4.7 V at *(G)* 500X, *(H)* 4000X, and *(F,I)* 10000X magnification.

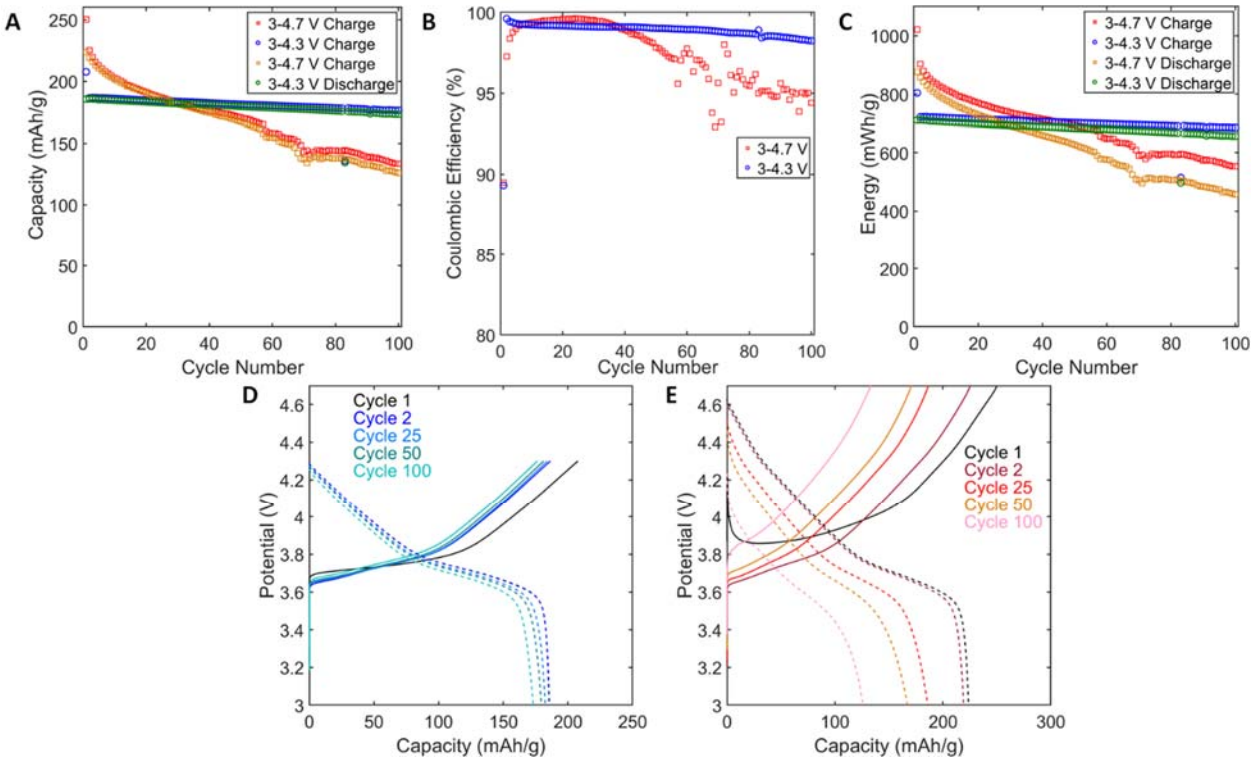

Figure 2. Galvanostatic cycling data of coin cells cycled 100 times. *(A)* (Dis)charge capacities, *(B)* Coulombic efficiencies, *(C)* (dis)charge energies, *(D)* (dis)charge curves of the cell cycled from 3-4.3 V, *(E)* (dis)charge curves of the cell cycled from 3-4.7 V. Charge curves are shown as solid lines and discharge curves are shown as dashed lines.

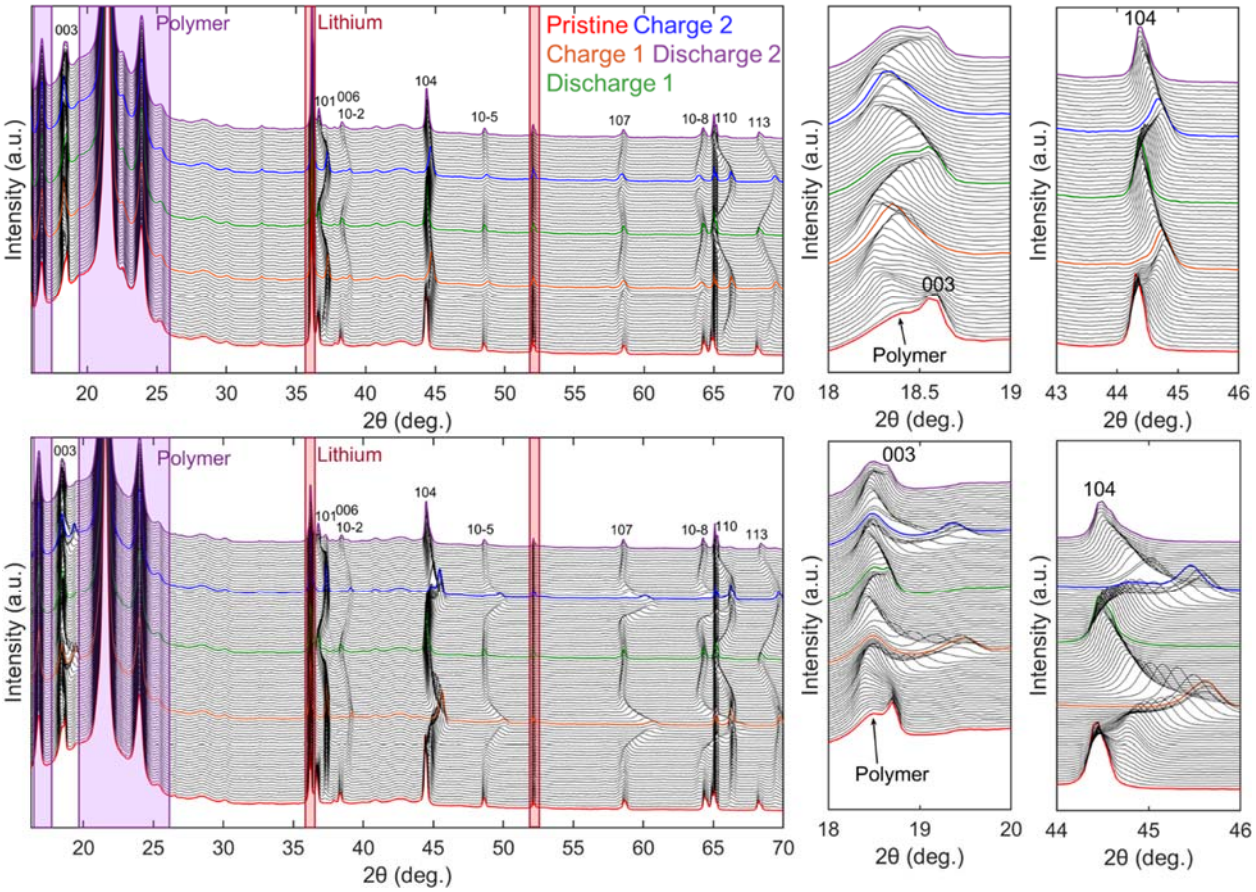

Figure 3. *Operando* XRD patterns of (*top*) cycles one and two of the 3-4.3 V cell and (*bottom*) cycles one and two of the 3-4.7 V cell. The pristine and fully (dis)charged scans are color-coded according the legend in the top panel and the insets of the (003) and (104) peaks are shown on the right.

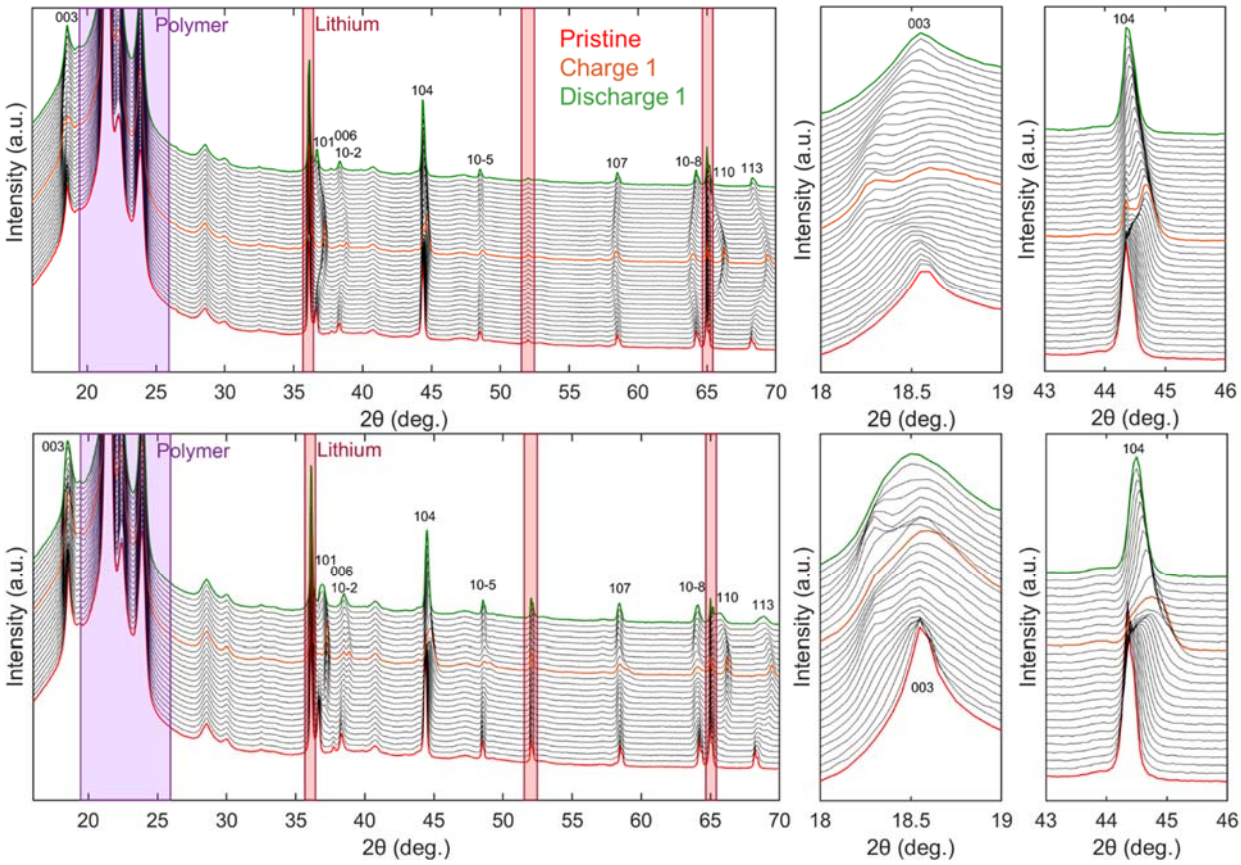

Figure 4. *Operando* XRD patterns of (*top*) cycle 101 of the 3-4.3 V cell and (*bottom*) cycles 101 of the 3-4.7 V cell. The pristine and fully (dis)charged scans are color-coded according the legend in the top panel and the insets of the (003) and (104) peaks are shown on the right.

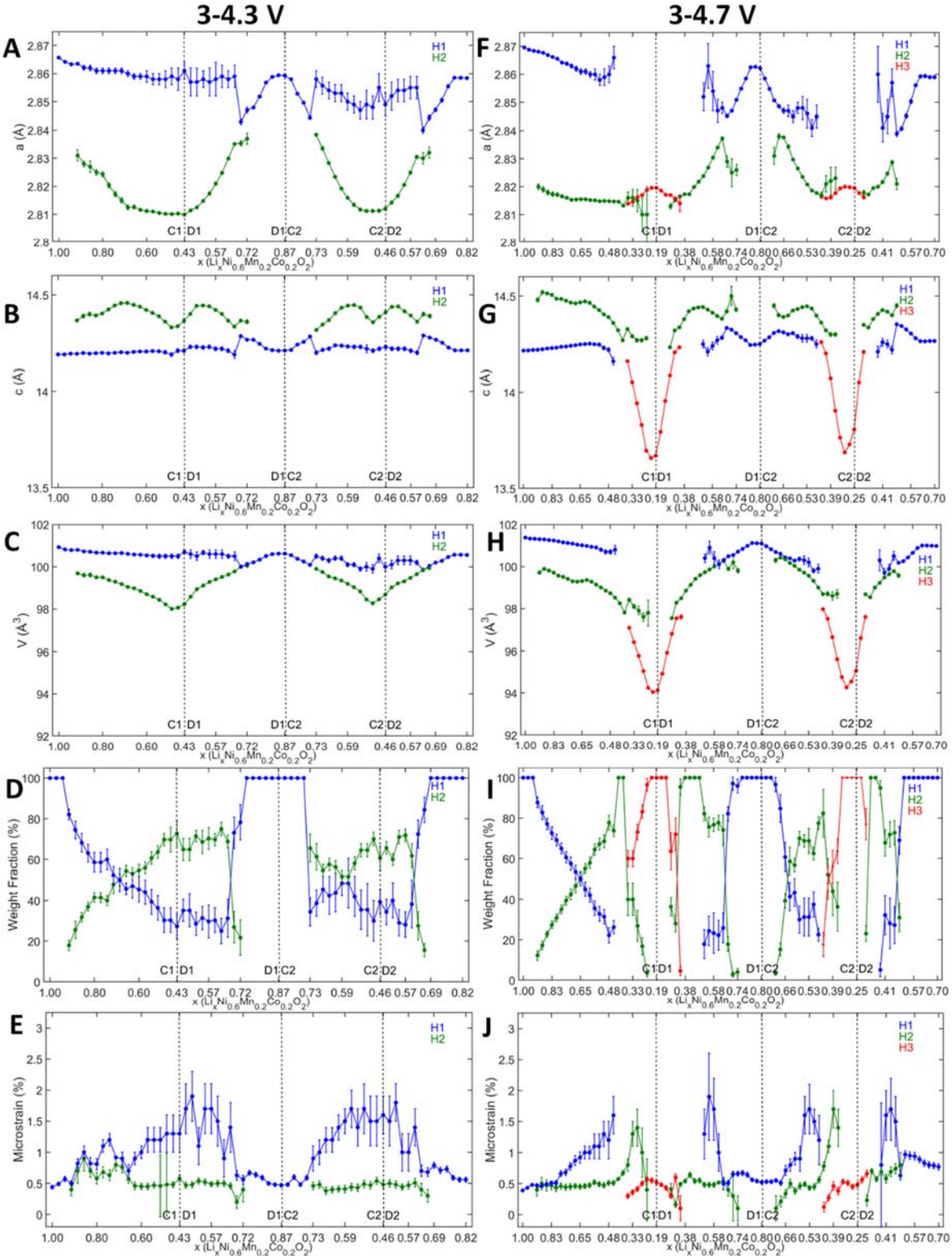

Figure 5. *(A)*, *(B)*, *(C)*, *(D)*, *(E)* are the *a* parameters, *c* parameters, volumes, weight fractions, and microstrains respectively for the XRD patterns collected on cycle one and two of the 3-4.3 V cell. *(F)*, *(G)*, *(H)*, *(I)*, *(J)* are the corresponding parameters for cycles one and two of the 3-4.7 V cell.

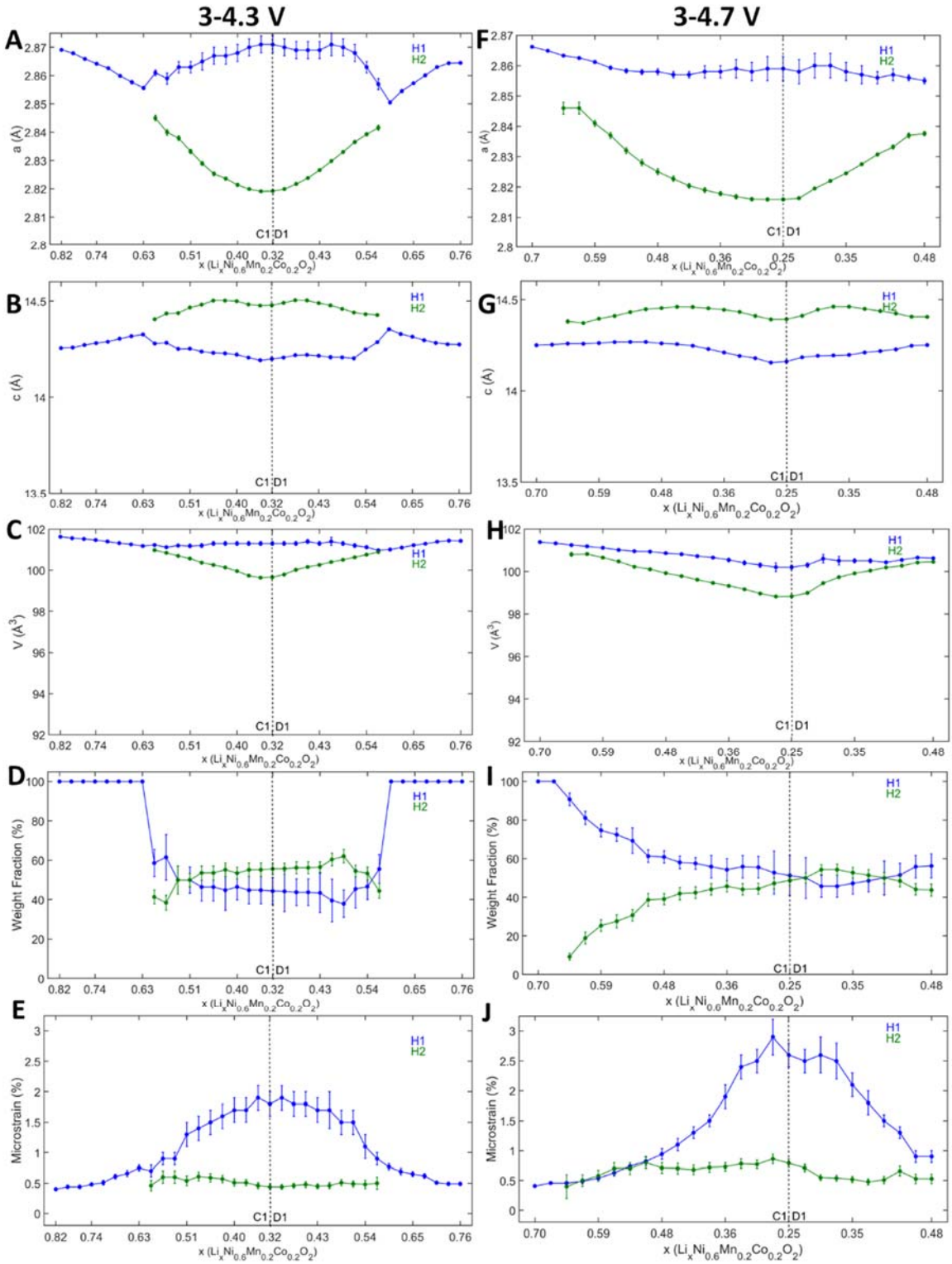

Figure 6. *(A)*, *(B)*, *(C)*, *(D)*, *(E)* are the *a* parameters, *c* parameters, volumes, weight fractions, and microstrains respectively for the XRD patterns collected on cycle 101 of the 3-4.3 V cell. *(F)*, *(G)*, *(H)*, *(I)*, *(J)* are the corresponding parameters for cycle 101 of the 3-4.7 V cell.

TOC Graphic

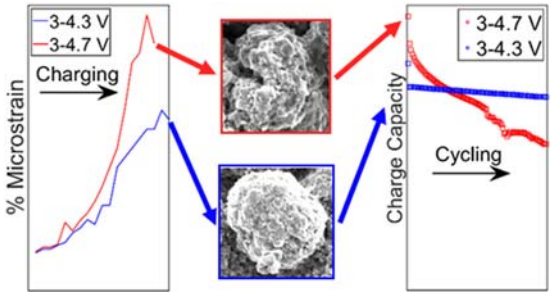
3-4.3 V
3-4.7 V
Charging
% Microstrain
3-4.7 V
3-4.3 V
Charge Capacity
Cycling

Supporting Information

Probing Sources of Capacity Fade in $LiNi_{0.6}Mn_{0.2}Co_{0.2}O_2$ (NMC622): An *Operando* XRD Study of Li/NMC622 Batteries During Extended Cycling

Calvin D. Quilty[1], David C. Bock[2], Shan Yan[2], Kenneth J. Takeuchi[1,3], Esther S. Takeuchi[1,2,3], Amy C. Marschilok[1,2,3]*

[1]Department of Chemistry, Stony Brook University, Stony Brook, New York 11794, United States

[2]Energy and Photon Sciences Directorate, Brookhaven National Laboratory, Upton, New York 11973, United States

[3]Department of Materials Science and Chemical Engineering, Stony Brook University, Stony Brook, New York 11794, United States

*Corresponding author: amy.marschilok@stonybrook.edu (ACM)

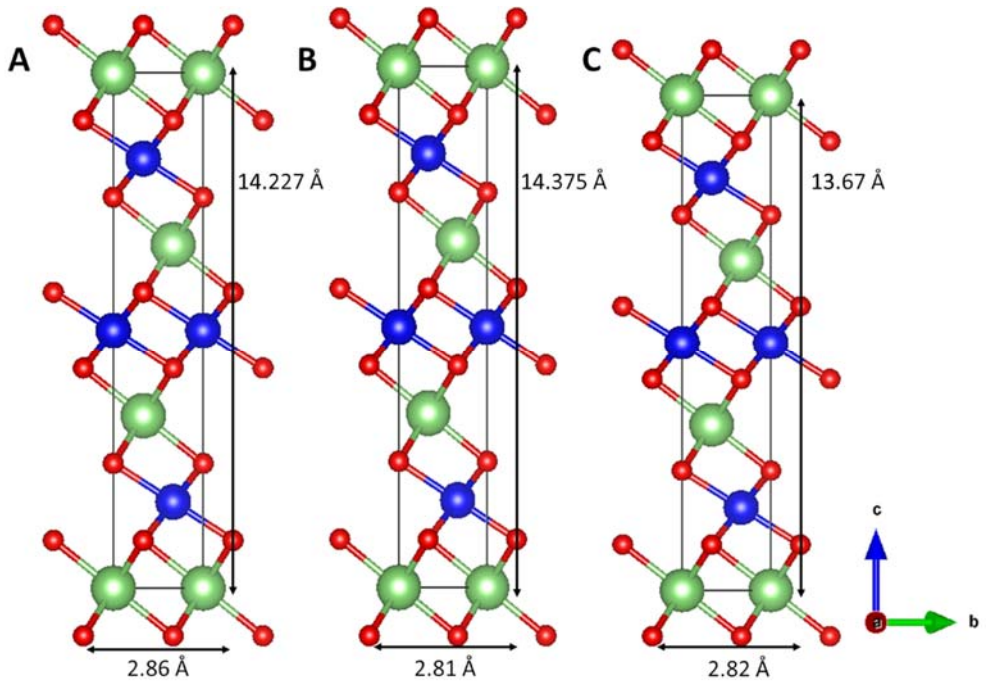

Figure S1. Crystal structures of the *(A)* H1, *(B)* H2, and *(C)* H3 phases of $LiNi_{ix}Mn_yCo_zO_2$, lithium is green, oxygen is red, and the Ni/Mn/Co is blue.

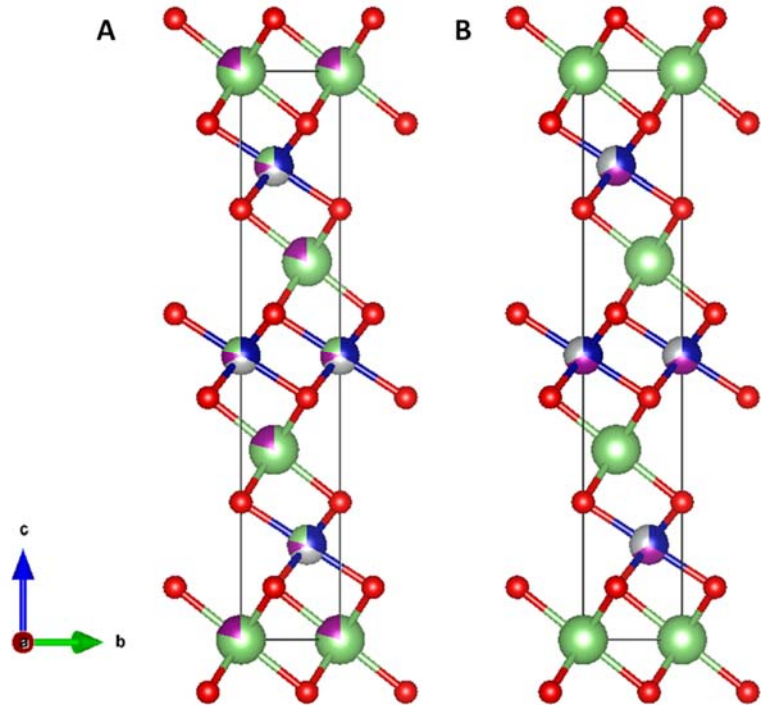

Figure S2. Crystal structure of NMC111 with Li-Ni site disorder *(A)* and without disorder *(B)*. Lithium is green, oxygen is red, nickel is purple, manganese is grey, and cobalt is blue.

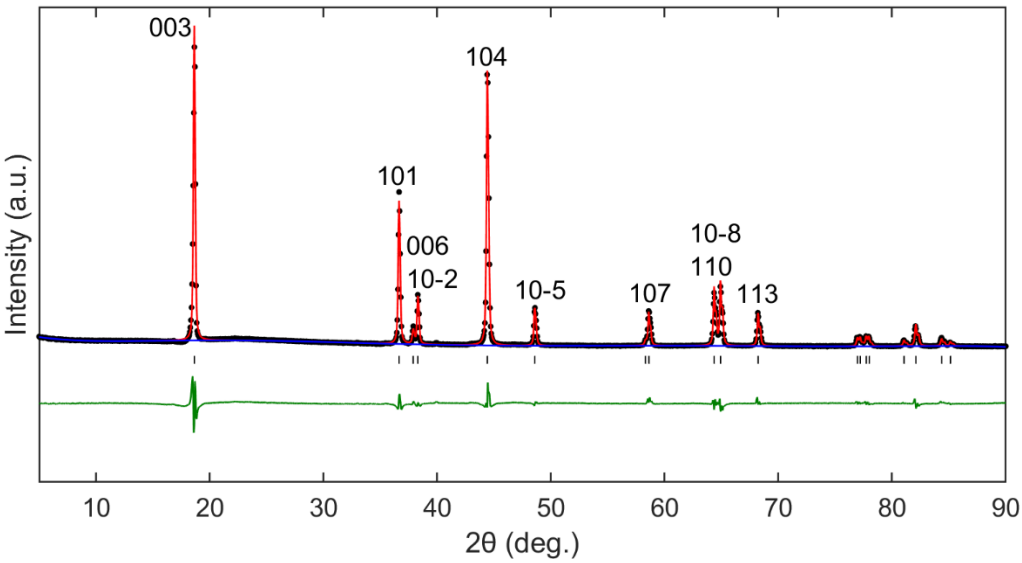

Figure S3. Rietveld refinement of NMC622. The data is in black, the calculated fit is in red, the background is in blue, and the difference is in green. The black lines correspond to the expected peak positions for NMC. The NMC peaks are indexed according to a prior structural report.[1]

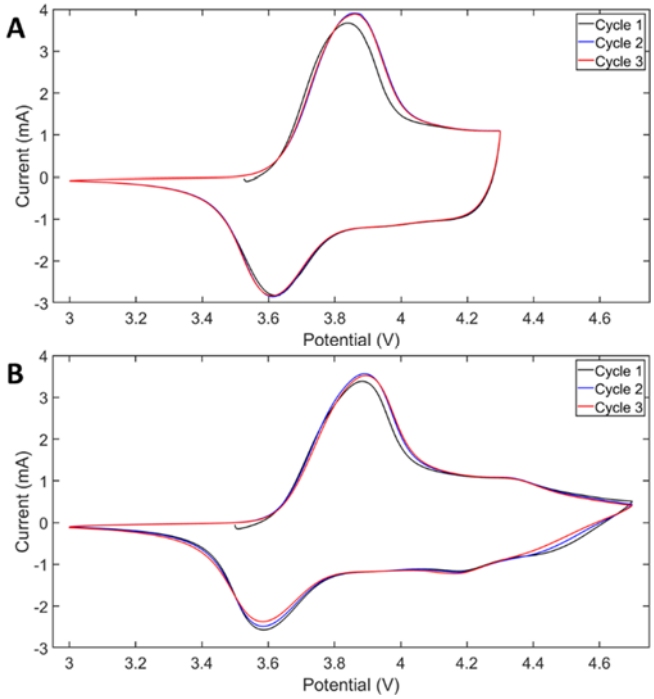

Figure S4. Cyclic voltammetry data of Li/NMC coin cells cycled from *(A)* 3-4.3 V and *(B)* 3-4.7 V.

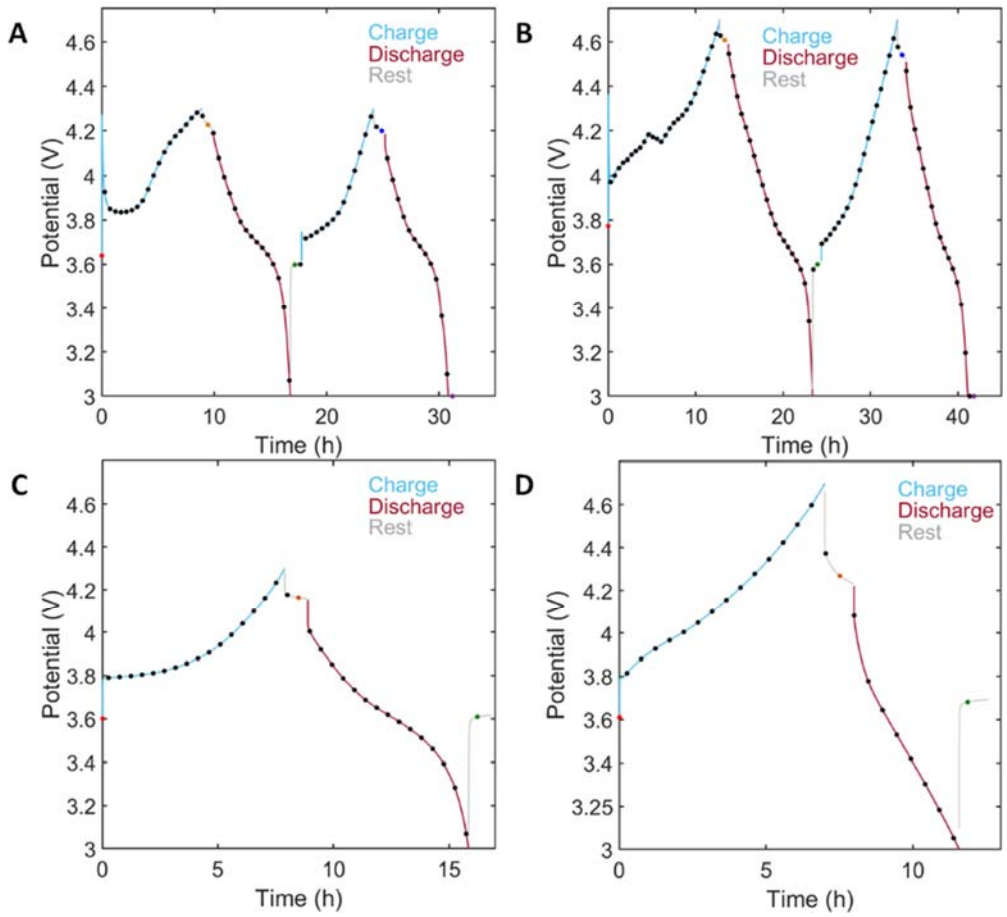

Figure S5. Galvanostatic cycling data of pouch cells used for operando measurements. The black points indicate when XRD scans were collected. The colored points indicate the key states of charge. *(A)* Cycles 1&2 for the 4.3 V cell, *(B)* cycles 1&2 for the 4.7 V cell, *(C)* cycle 101 for the 4.3 V cell, and *(D)* cycle 101 for the 4.7 V cell.

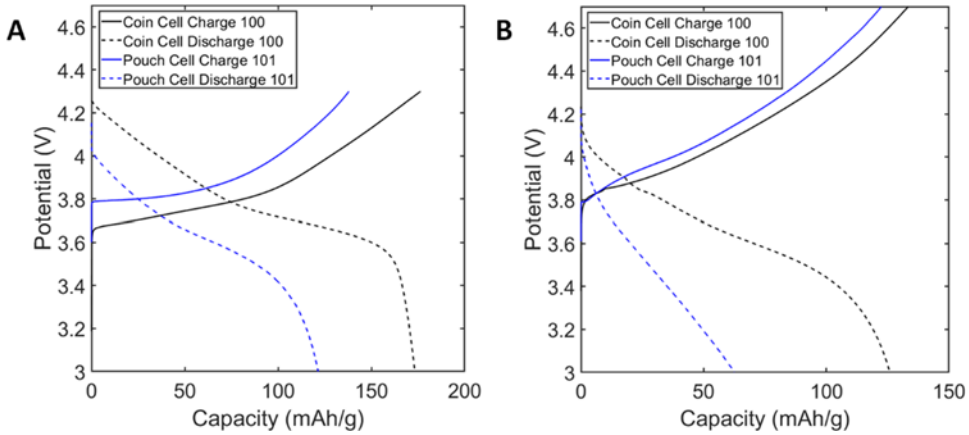

Figure S6. Galvanostatic cycling for coin cells at cycle 100 and pouch cells at cycle 101. *(A)* Cells cycled from 3-4.3 V, and *(B)* cells cycled from 3-4.7 V.

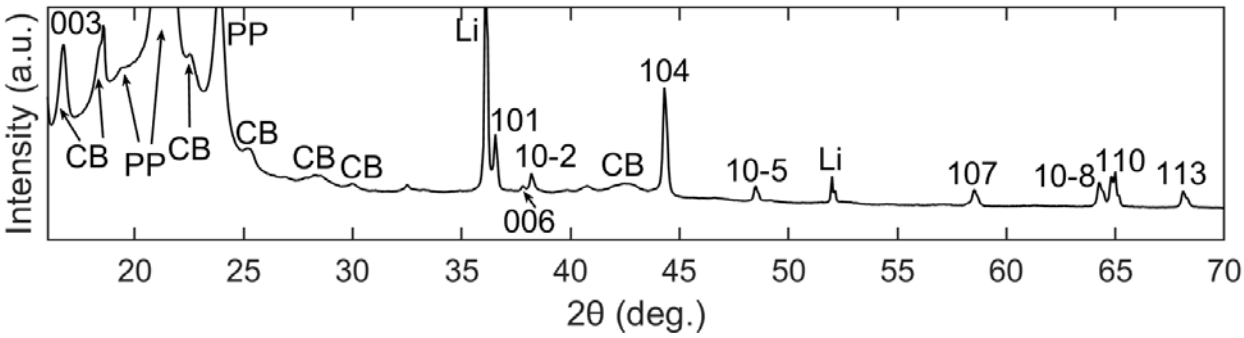

Figure S7. XRD pattern of the 3-4.3 V pouch cell prior to cycling. Peaks labelled as Li, CB, and PP correspond to lithium, the cell block, and polypropylene respectively.

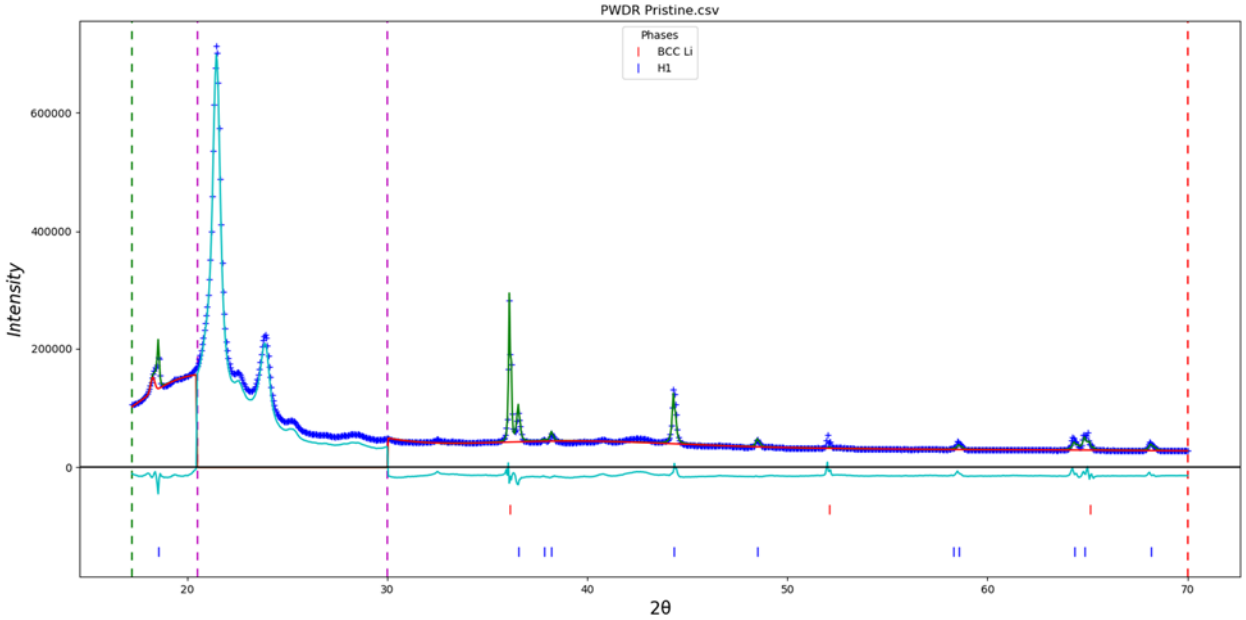

Figure S8. Rietveld refinement of the XRD pattern collected on the 3-4.3 V NMC622 pouch cell prior to cycling. The blue points mark the experimental data, the green line is the calculated fit, the red line is the background, and the light blue line is the difference between the observed and the calculated data. The background peak at 18.3° was consistent with a peak associated with the cell block and was used for all cycle 1 and 2 refinements. $\%R_{wp}$=4.30.

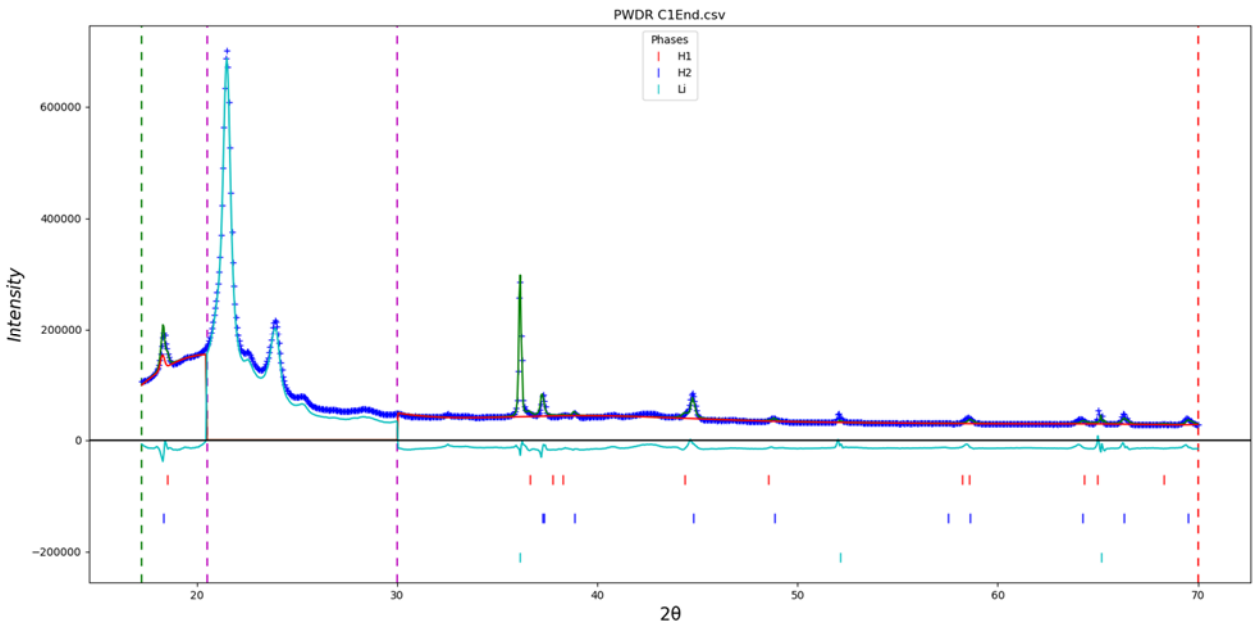

Figure S9. Rietveld refinement of the XRD pattern collected on the 3-4.3 V NMC622 pouch cell at the end of the 1st charge. The blue points mark the experimental data, the green line is the calculated fit, the red line is the background, and the light blue line is the difference between the observed and the calculated data. %R_{wp}=4.49.

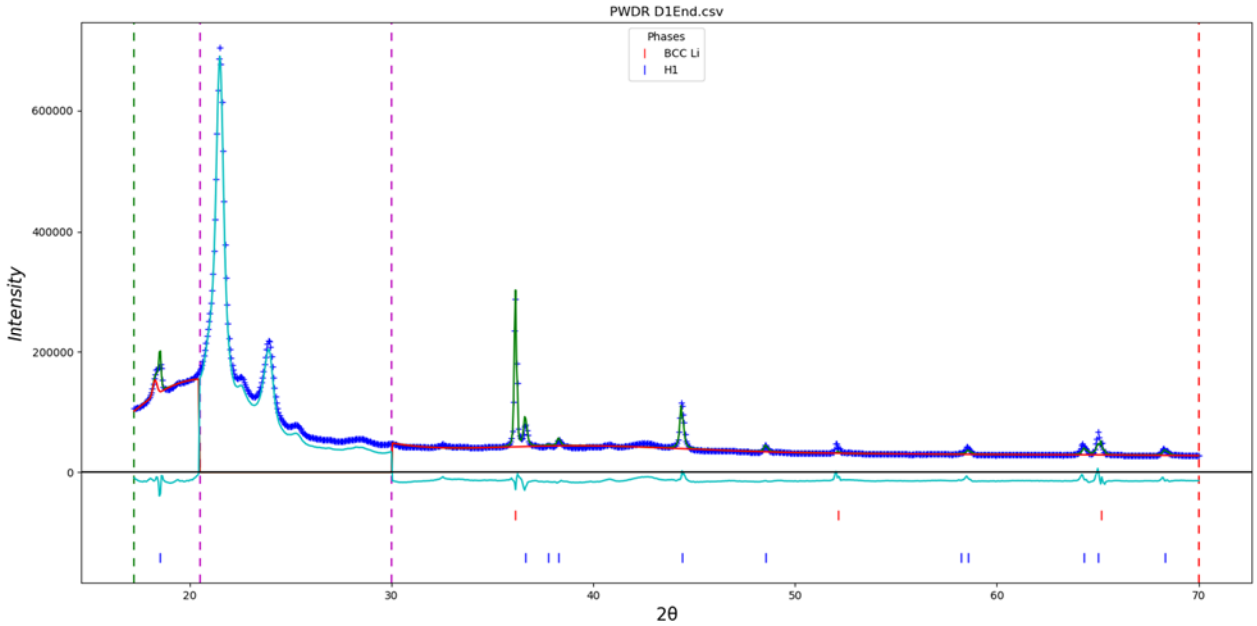

Figure S10. Rietveld refinement of the XRD pattern collected on the 3-4.3 V NMC622 pouch cell at the end of the 1st discharge. The blue points mark the experimental data, the green line is the calculated fit, the red line is the background, and the light blue line is the difference between the observed and the calculated data. %R_{wp}=4.20.

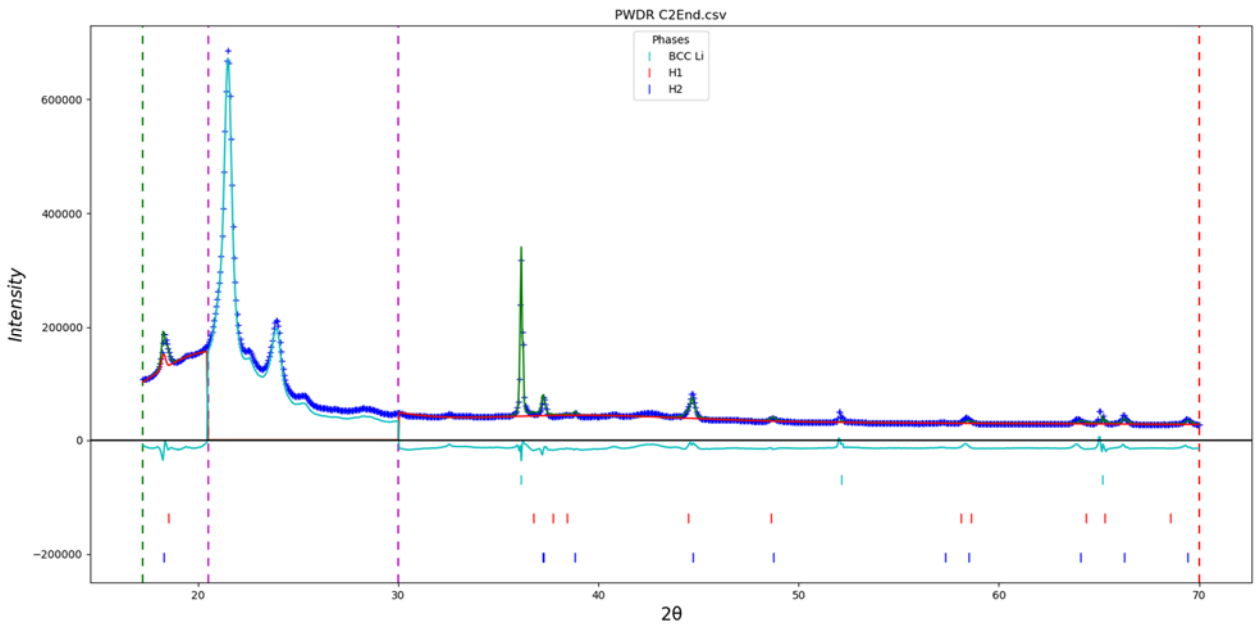

Figure S11. Rietveld refinement of the XRD pattern collected on the 3-4.3 V NMC622 pouch cell at the end of the 2nd charge. The blue points mark the experimental data, the green line is the calculated fit, the red line is the background, and the light blue line is the difference between the observed and the calculated data. %R_{wp}=4.45.

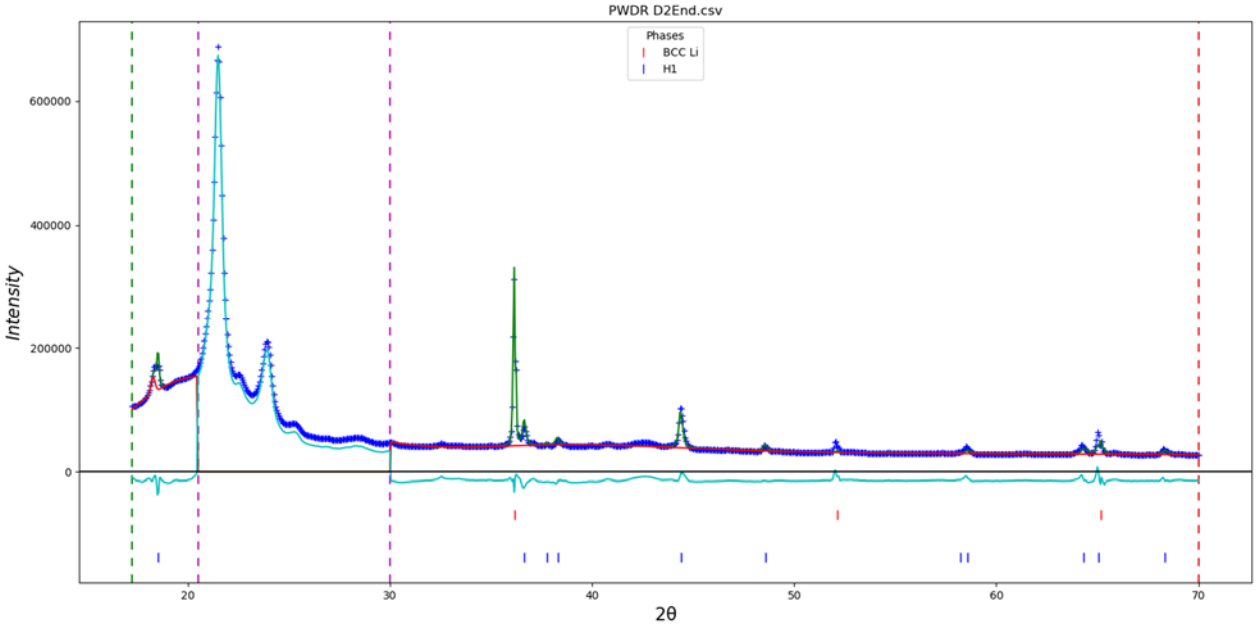

Figure S12. Rietveld refinement of the XRD pattern collected on the 3-4.3 V NMC622 pouch cell at the end of the 2nd discharge. The blue points mark the experimental data, the green line is the calculated fit, the red line is the background, and the light blue line is the difference between the observed and the calculated data. %R_{wp}=4.27.

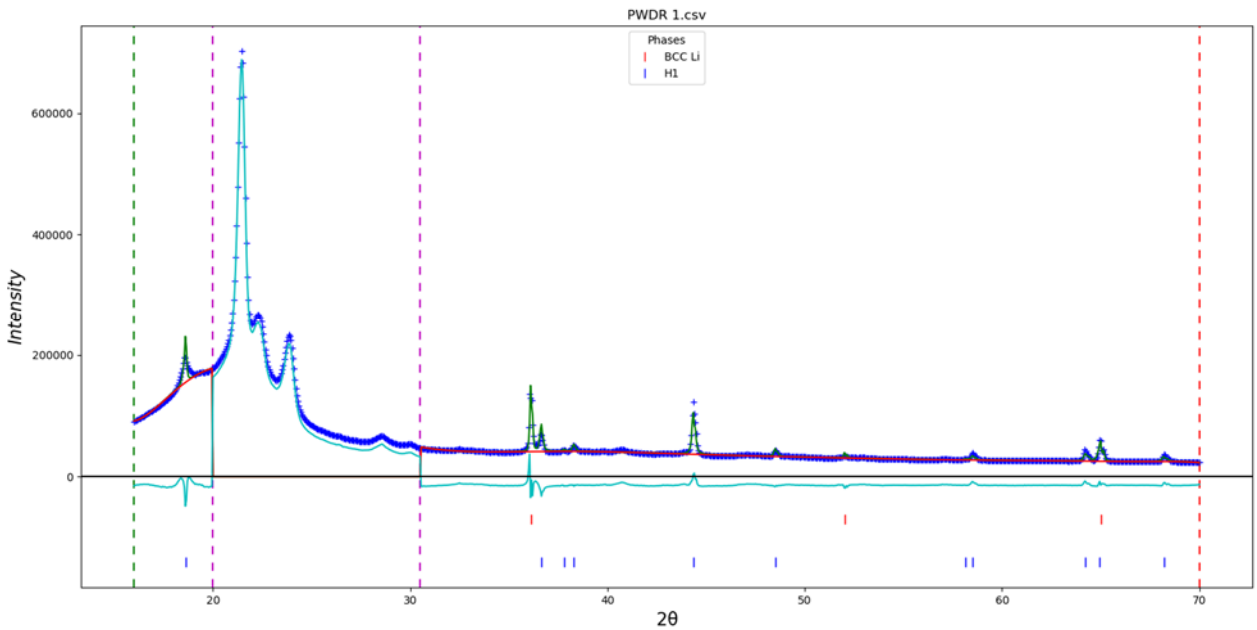

Figure S13. Rietveld refinement of the XRD pattern collected on the 3-4.3 V NMC622 pouch cell prior to the 101st cycle. The blue points mark the experimental data, the green line is the calculated fit, the red line is the background, and the light blue line is the difference between the observed and the calculated data. A background peak was not used for the cycle 101 refinements as a less diffracting cell block was used. $\%R_{wp}$=3.90.

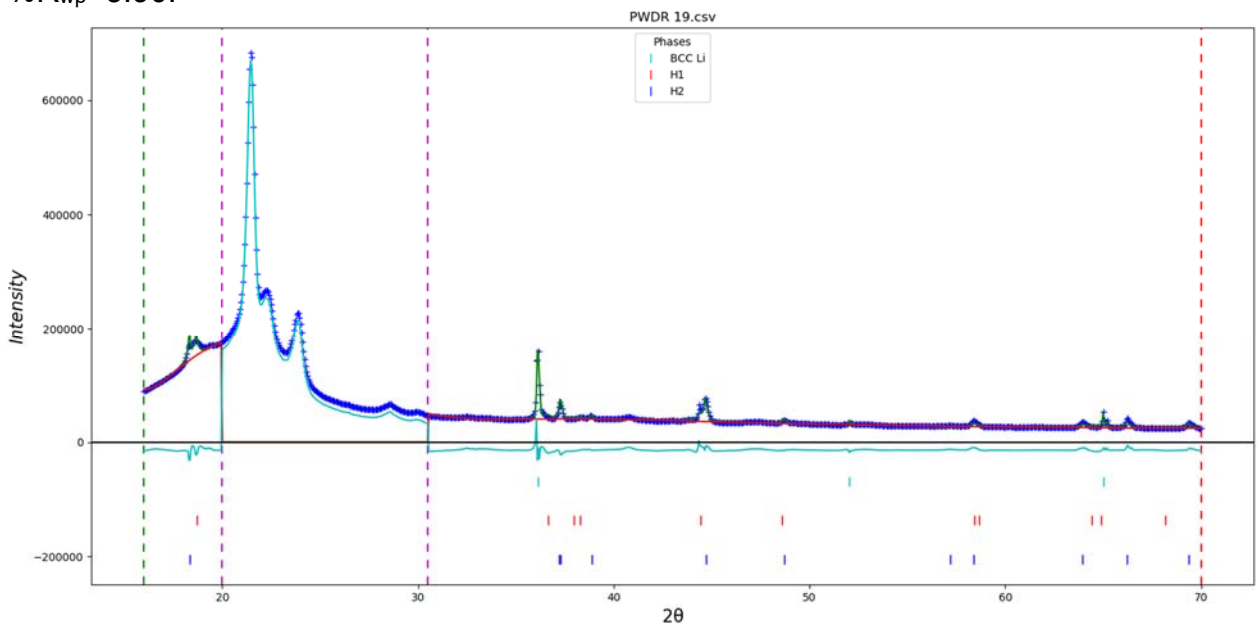

Figure S14. Rietveld refinement of the XRD pattern collected on the 3-4.3 V NMC622 pouch cell at the end of the 101st charge. The blue points mark the experimental data, the green line is the calculated fit, the red line is the background, and the light blue line is the difference between the observed and the calculated data. $\%R_{wp}$=3.61.

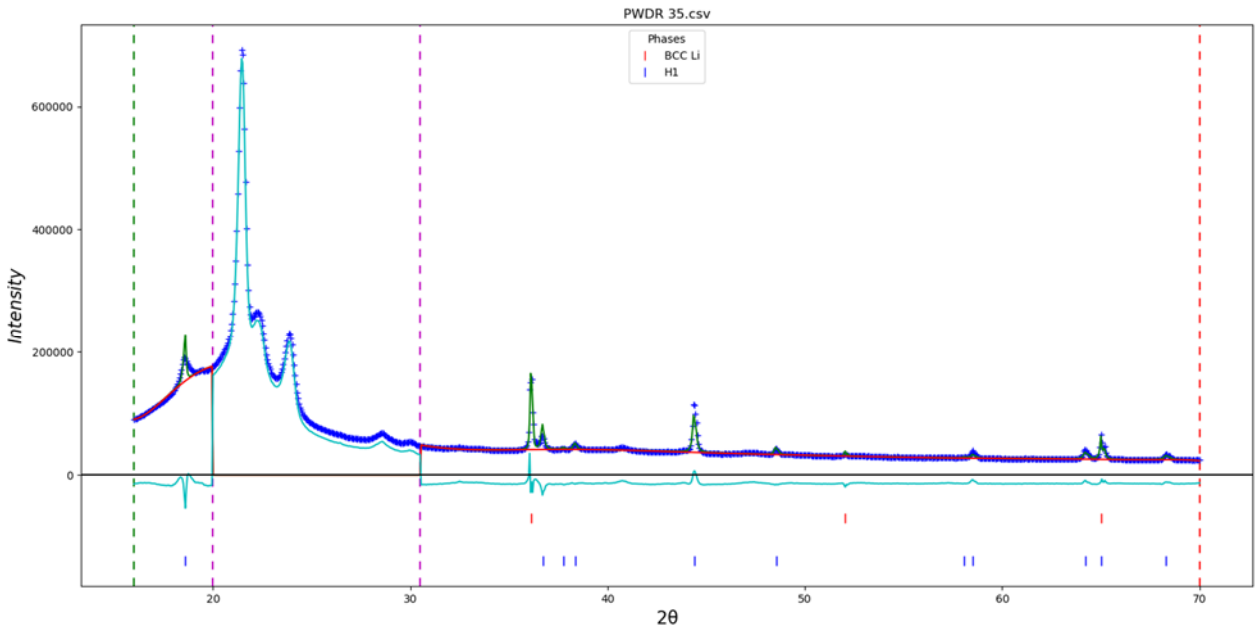

Figure S15. Rietveld refinement of the XRD pattern collected on the 3-4.3 V NMC622 pouch cell at the end of the 101st discharge. The blue points mark the experimental data, the green line is the calculated fit, the red line is the background, and the light blue line is the difference between the observed and the calculated data. $\%R_{wp}$=3.80.

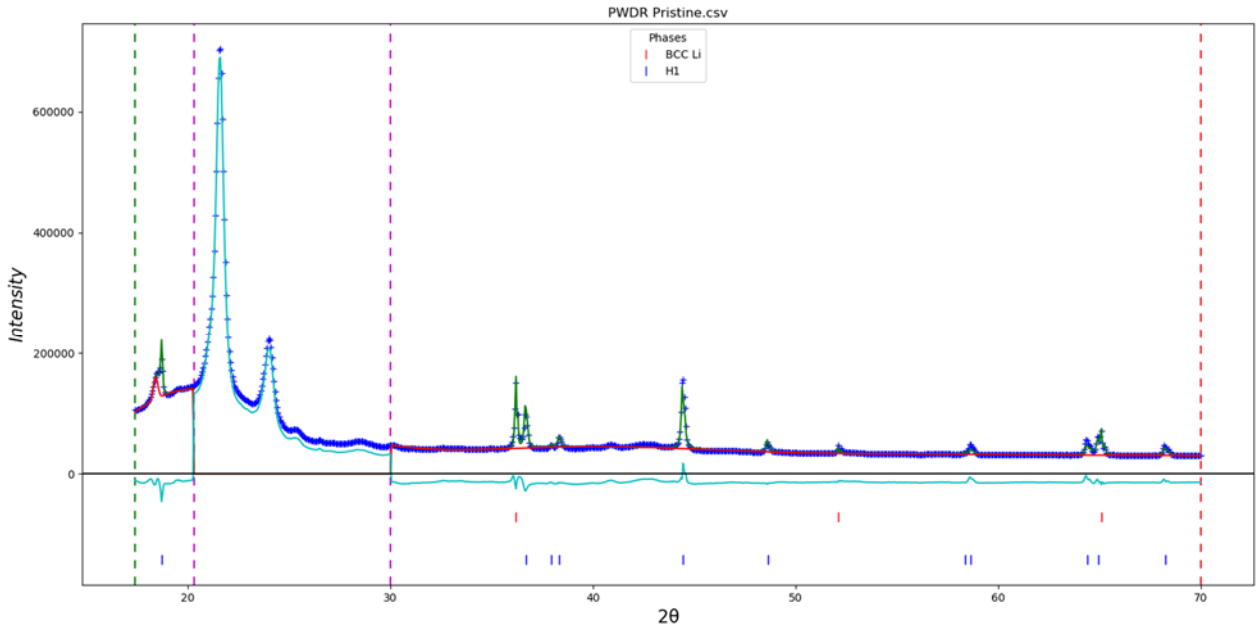

Figure S16. Rietveld refinement of the XRD pattern collected on the 3-4.7 V NMC622 pouch cell prior to cycling. The blue points mark the experimental data, the green line is the calculated fit, the red line is the background, and the light blue line is the difference between the observed and the calculated data. $\%R_{wp}$=3.78.

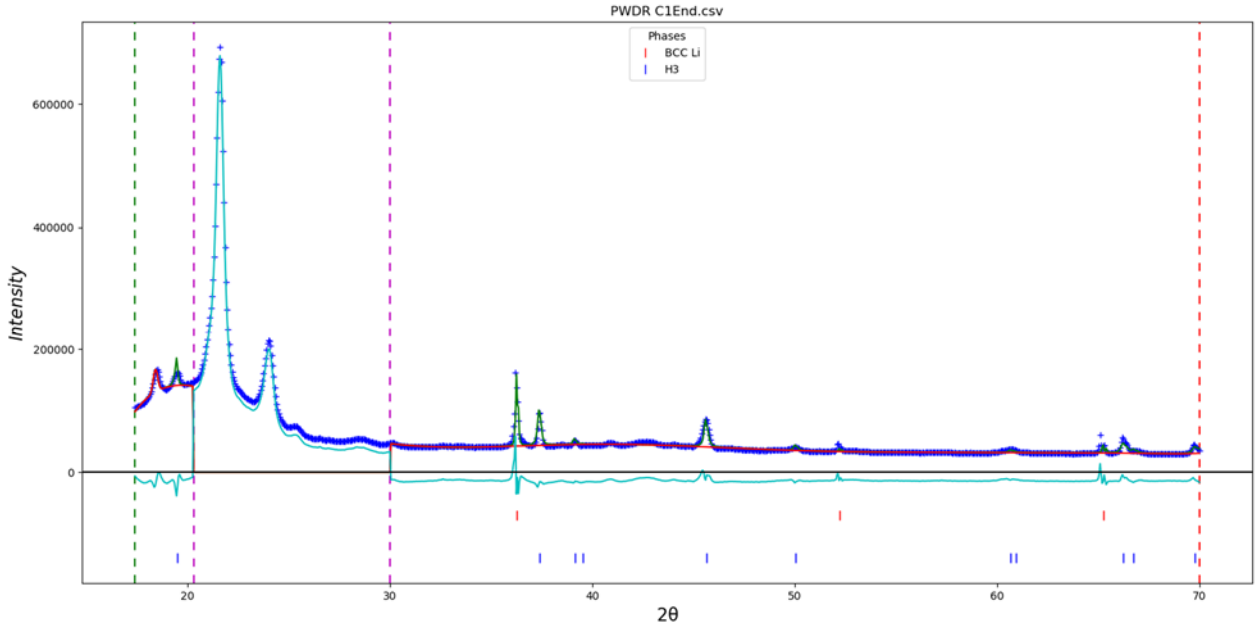

Figure S17. Rietveld refinement of the XRD pattern collected on the 3-4.7 V NMC622 pouch cell at the end of the 1st charge. The blue points mark the experimental data, the green line is the calculated fit, the red line is the background, and the light blue line is the difference between the observed and the calculated data. %R_{wp}=5.31.

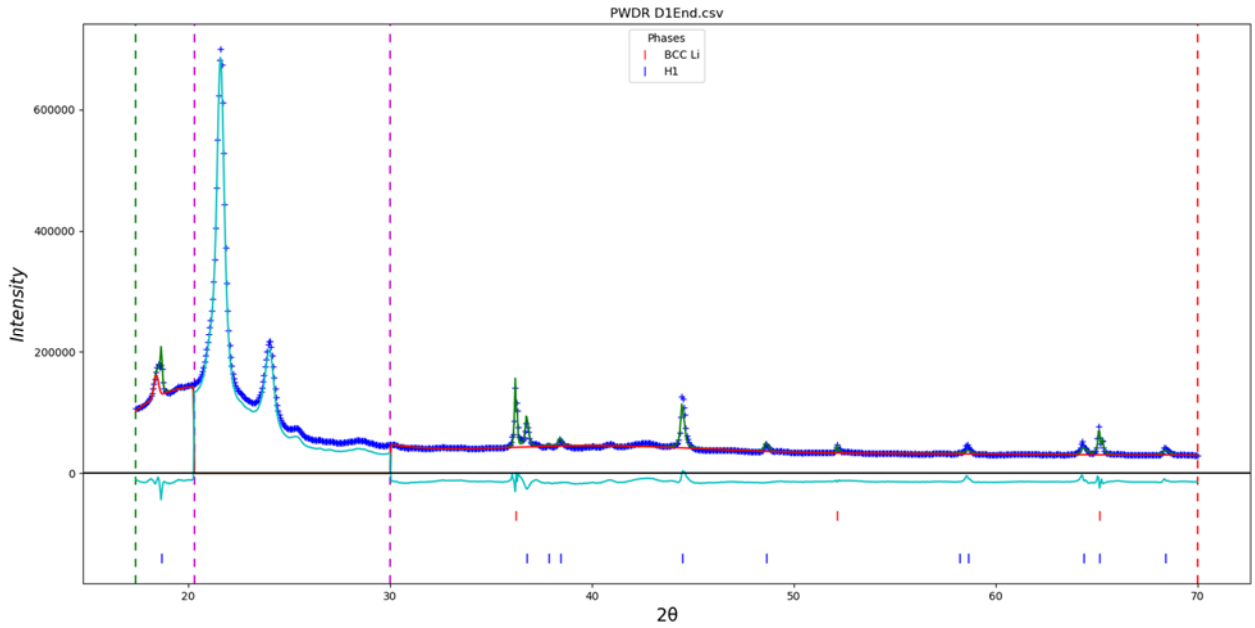

Figure S18. Rietveld refinement of the XRD pattern collected on the 3-4.7 V NMC622 pouch cell at the end of the 1st discharge. The blue points mark the experimental data, the green line is the calculated fit, the red line is the background, and the light blue line is the difference between the observed and the calculated data. %R_{wp}=3.90.

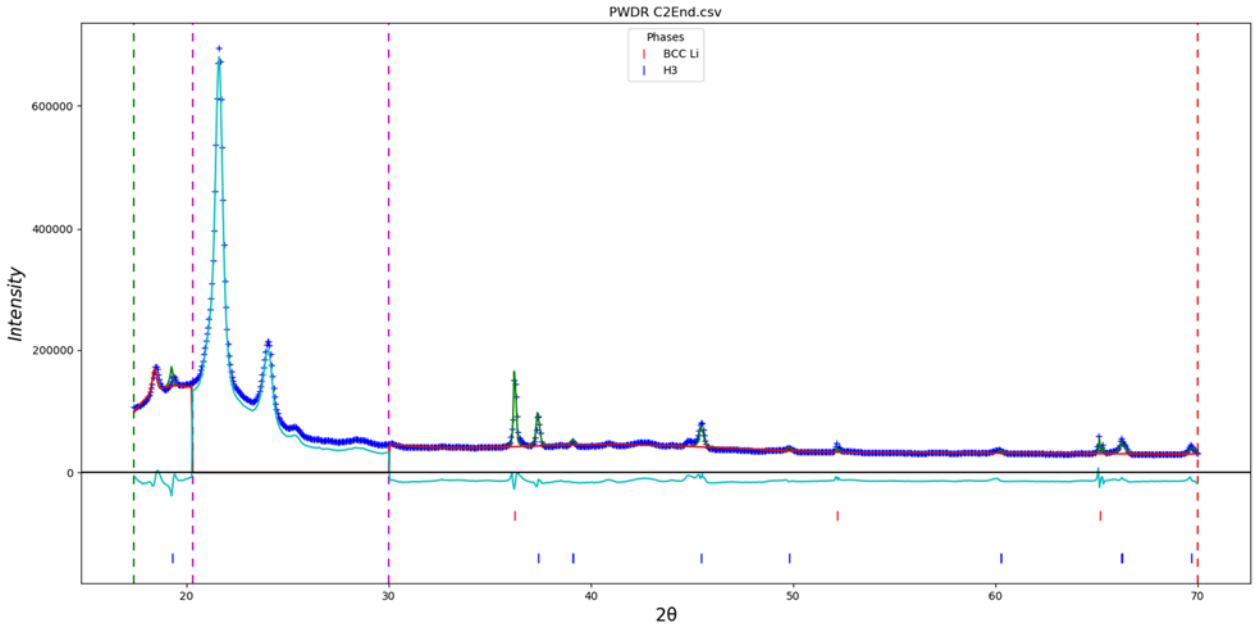

Figure S19. Rietveld refinement of the XRD pattern collected on the 3-4.7 V NMC622 pouch cell at the end of the 2nd charge. The blue points mark the experimental data, the green line is the calculated fit, the red line is the background, and the light blue line is the difference between the observed and the calculated data. %R_{wp}=4.30.

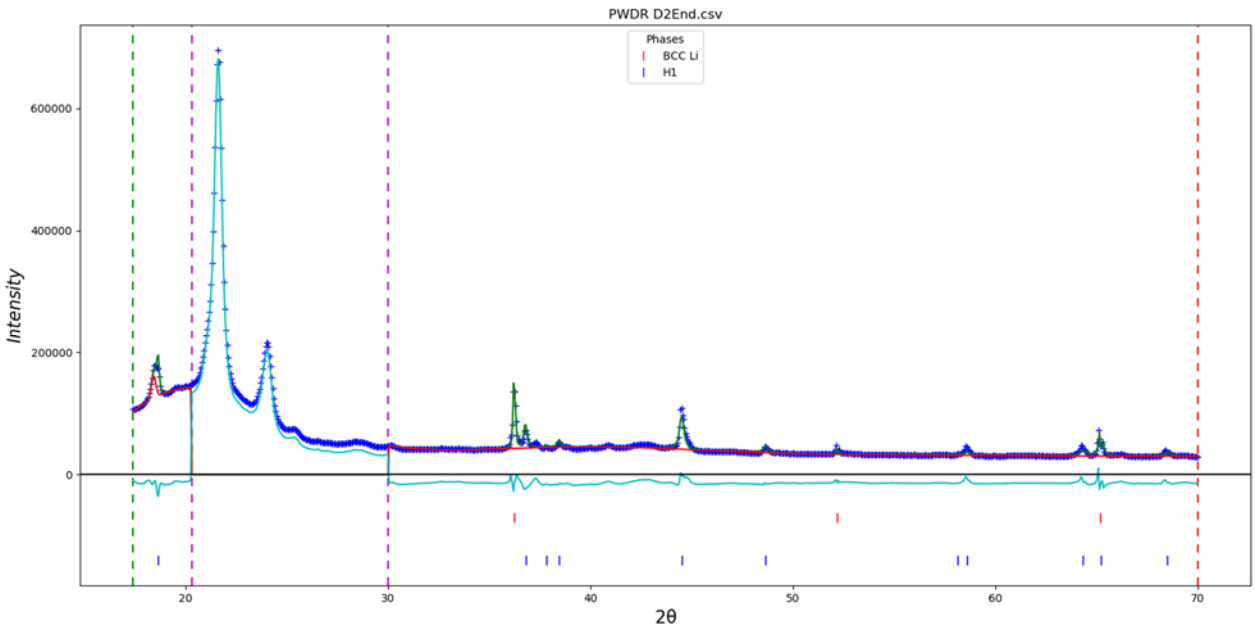

Figure S20. Rietveld refinement of the XRD pattern collected on the 3-4.7 V NMC622 pouch cell at the end of the 2nd discharge. The blue points mark the experimental data, the green line is the calculated fit, the red line is the background, and the light blue line is the difference between the observed and the calculated data. %R_{wp}=4.20.

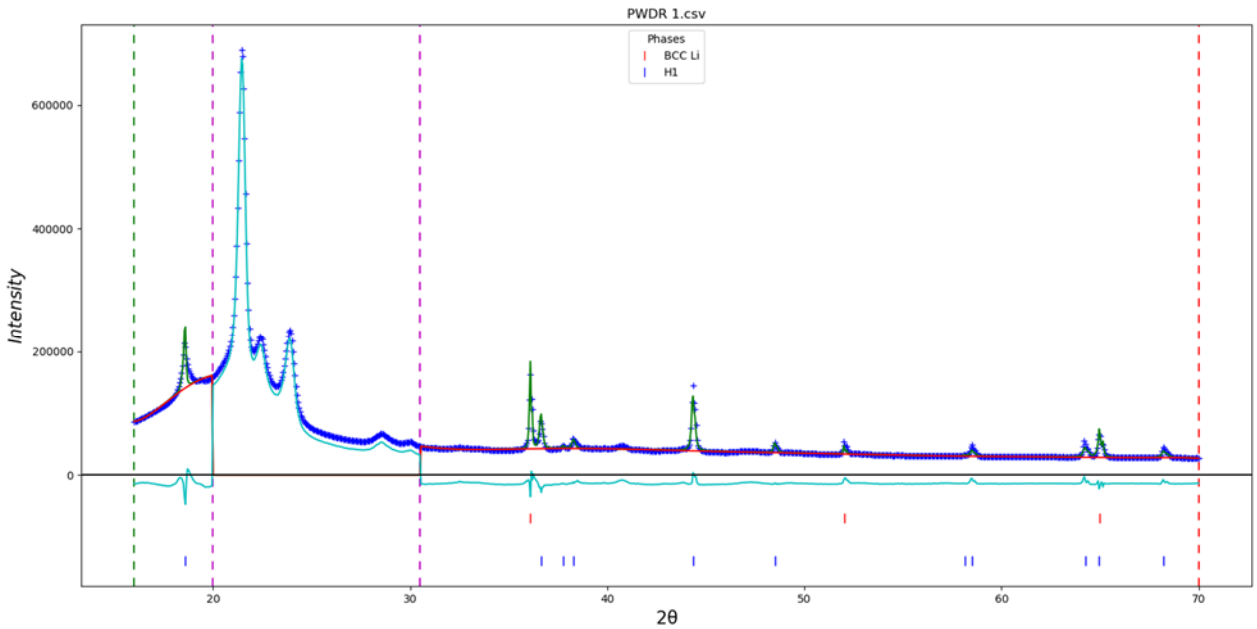

Figure S21. Rietveld refinement of the XRD pattern collected on the 3-4.7 V NMC622 pouch cell prior to the 101st cycle. The blue points mark the experimental data, the green line is the calculated fit, the red line is the background, and the light blue line is the difference between the observed and the calculated data. %R_{wp}=3.64

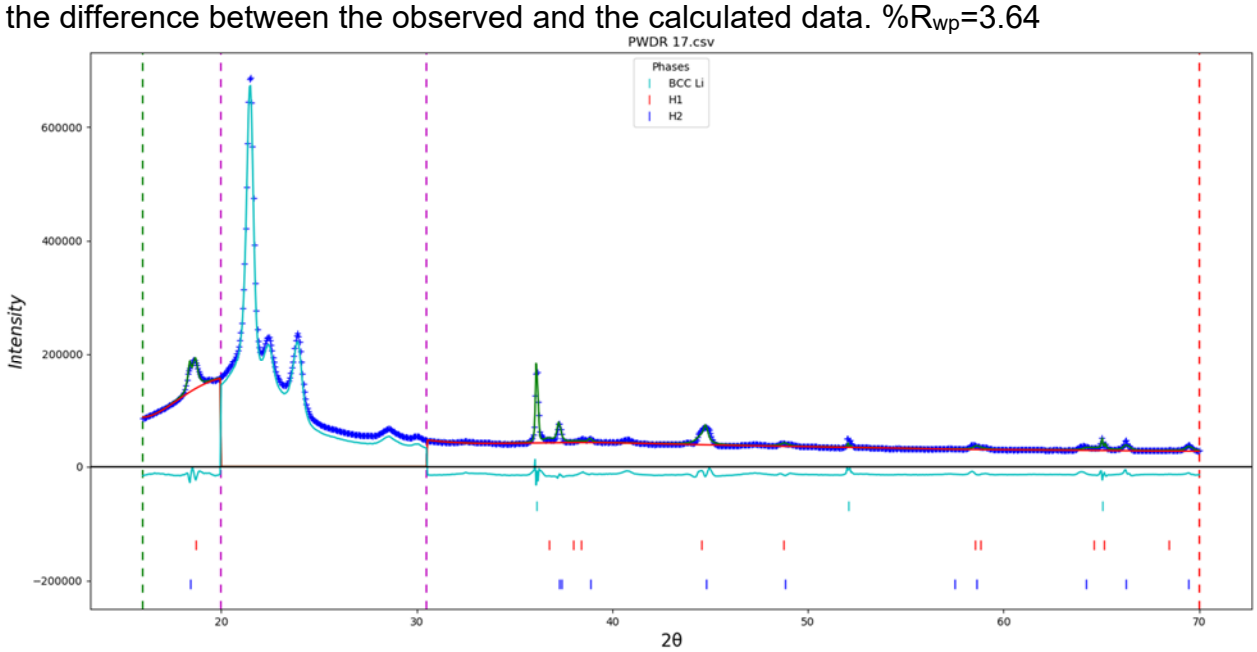

Figure S22. Rietveld refinement of the XRD pattern collected on the 3-4.7 V NMC622 pouch cell at the end of the 101st charge. The blue points mark the experimental data, the green line is the calculated fit, the red line is the background, and the light blue line is the difference between the observed and the calculated data. %R_{wp}=3.50.

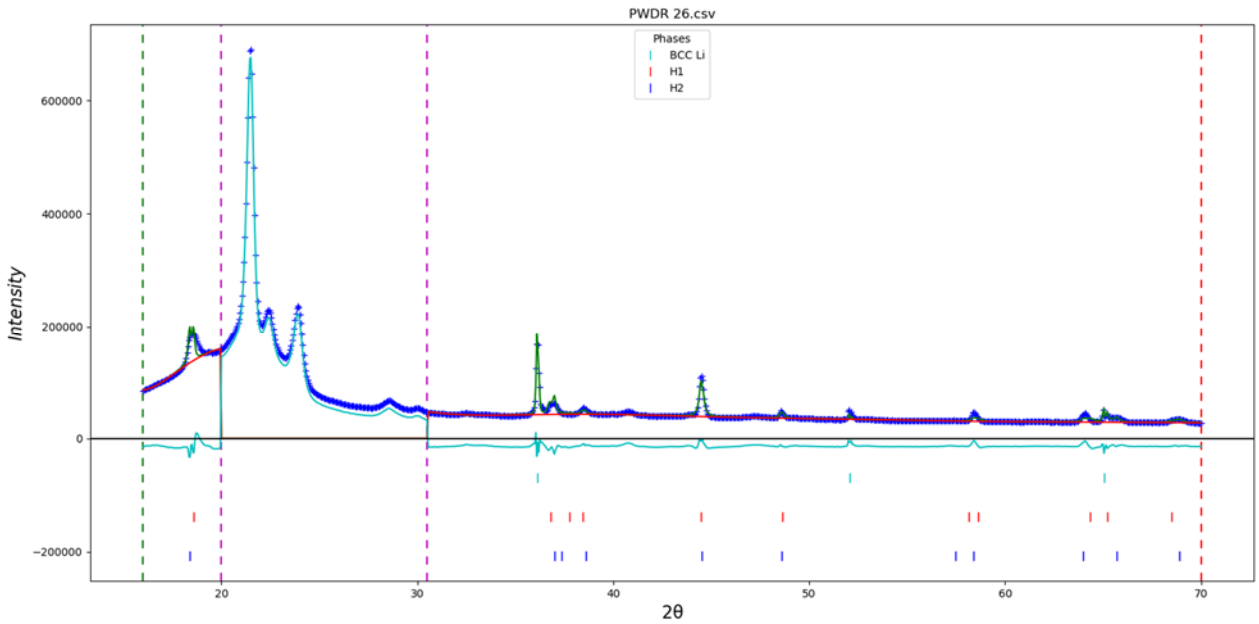

Figure S23. Rietveld refinement of the XRD pattern collected on the 3-4.7 V NMC622 pouch cell at the end of the 101st discharge. The blue points mark the experimental data, the green line is the calculated fit, the red line is the background, and the light blue line is the difference between the observed and the calculated data. $\%R_{wp}$=3.92.

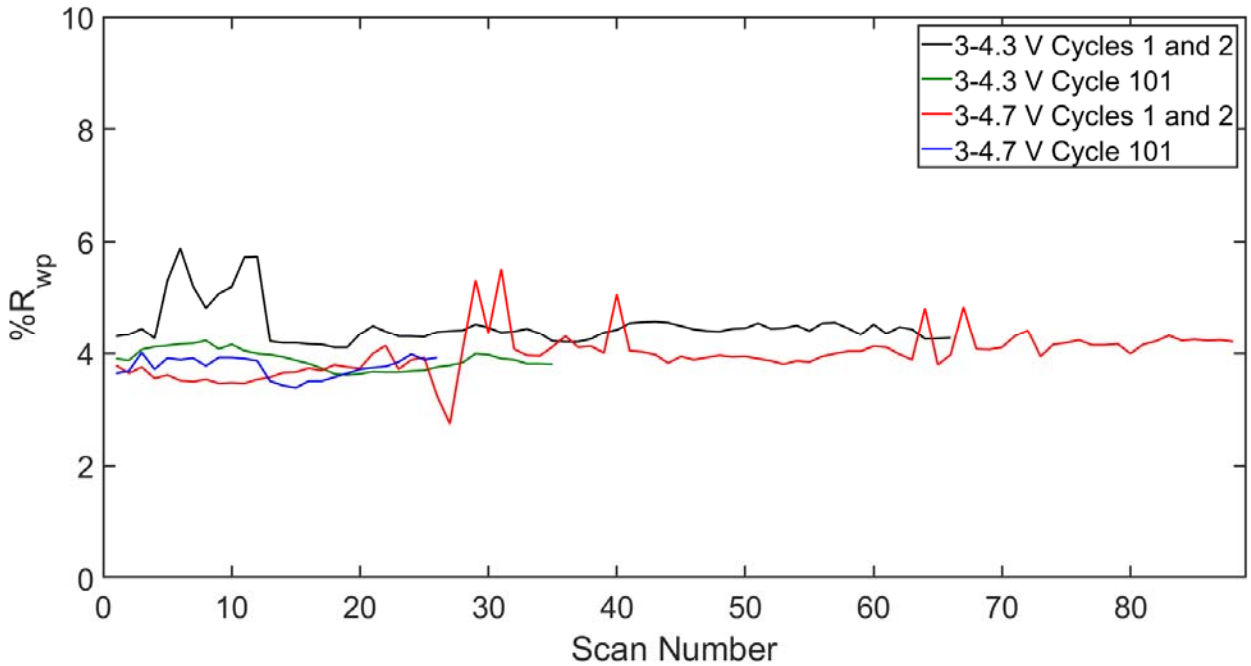

Figure S24 $\%R_{wp}$ values for the Rietveld refinements. *(A)* Values for cycles 1 and 2 of the 3-4.3 V cell, *(B)* Values for cycle 101 of the 3-4.3 V cell, *(C)* Values for cycles 1 and 2 of the 3-4.7 V cell, and *(D)* Values for cycle 101 of the 3-4.7 V cell.

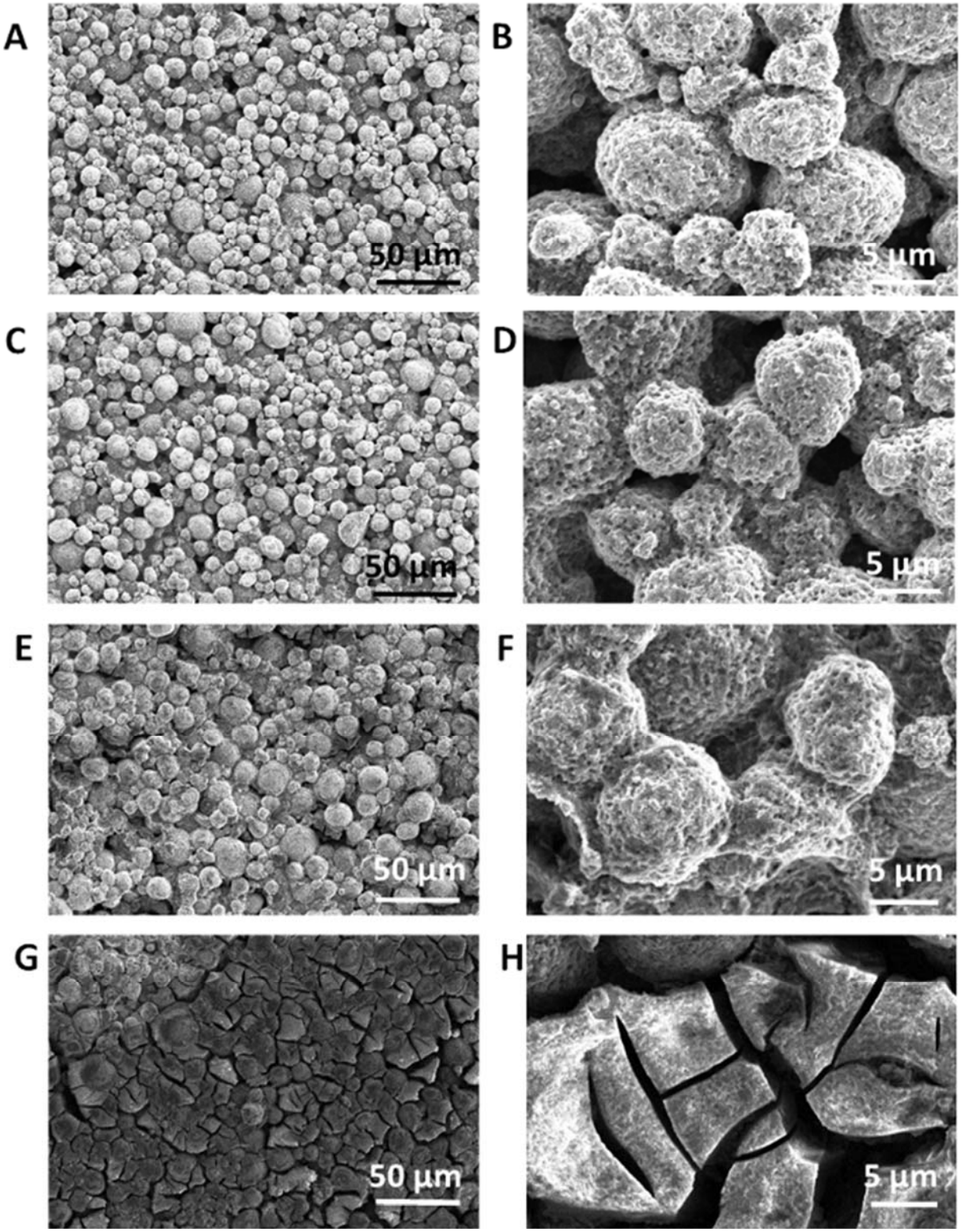

Figure S25. SEM images of an electrode cycled 100 times at 3-4.3 V at *(A,C)* 500X and *(B,D)* 4000X magnification. Images of an electrode cycled 100 times at 3-4.7 V at *(E,G)* 500X and *(F,H)* 4000X magnification.

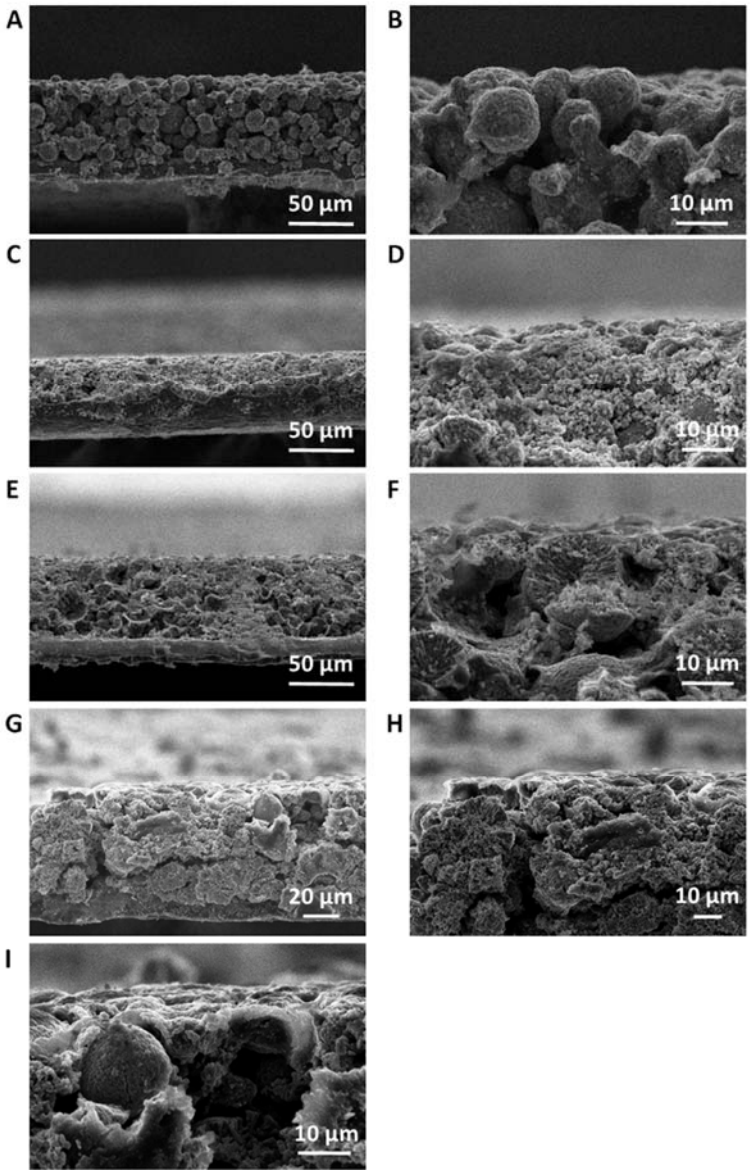

Figure S26. Cross sectional SEM images of a pristine NMC622 electrode at *(A)* 500X and *(B)* 2000X magnification. Images of an electrode cycled 100 times at 3-4.3 V at *(C)* 500X and *(D)* 2000X magnification. Images of an electrode cycled 100 times at 3-4.7 V at *(E)* 500X, *(F)* 2000X, *(G)* 650X, *(H)* 1000X, and *(I)* 2000X magnification

Table S1. Coin cell electrochemistry for cells cycled one hundred times at either 3-4.7 V or 3-4.3 V. Values are reported as Mean(SD). Capacities (cap.) are in mAh/g, charge is abbreviated C, discharge is abbreviated D, and CE is Coulombic efficiency.

Window	**C1 cap.**	**D1 cap.**	**Cycle 1 CE**	**C2 cap.**	**D2 cap.**
3-4.3 V	208(2)	186(2)	89.30(8)%	187(1)	186(1)
3-4.7 V	249(7)	224(7)	90.1(4)%	224(7)	221(7)
Window	**Cycle 2 CE**	**C100 cap.**	**D100 cap.**	**Cycle 100 CE**	**Cap. fade (cycle 2→100)**
3-4.3 V	99.60(8)%	175(2)	170(2)	97(1)%	6(1)%
3-4.7 V	98.5(8)%	100(20)	100(20)	93(1)%	50(10)%

References

1. Yin, S. C.; Rho, Y. H.; Swainson, I.; Nazar, L. F., X-Ray/Neutron Diffraction and Electrochemical Studies of Lithium De/Re-Intercalation in Li1-Xco1/3ni1/3mn1/3o2 (X = 0 → 1). *Chem. Mater.* **2006**, *18*, 1901-1910.